

1 **Simulating Wildfire Emissions and Plumerise using**  
2 **Geostationary Satellite Fire Radiative Power**  
3 **Measurements: A Case Study of the 2019 Williams**  
4 **Flats fire**

5 Aditya Kumar<sup>1\*</sup>, R. Bradley Pierce<sup>1</sup>, Ravan Ahmadov<sup>2,3</sup>, Gabriel  
6 Pereira<sup>4</sup>, Saulo Freitas<sup>5</sup>, Georg Grell<sup>3</sup>, Chris Schmidt<sup>1</sup>, Allen Lenzen<sup>1</sup>,  
7 Joshua P. Schwarz<sup>6</sup>, Anne E. Perring<sup>7</sup>, Joseph M. Katich<sup>7,8</sup>, John Hair<sup>9</sup>,  
8 Jose L. Jimenez<sup>2, 10</sup>, Pedro Campuzano-Jost<sup>2, 10</sup>, Hongyu Guo<sup>2,10</sup>

9 <sup>1</sup>Space Science and Engineering Center, University of Wisconsin Madison,  
10 Madison, WI

11 <sup>2</sup>Cooperative Institute for Research in Environmental Sciences (CIRES),  
12 University of Colorado Boulder, Boulder, CO

13 <sup>3</sup>NOAA Global Systems Laboratory, Boulder, CO

14 <sup>4</sup>Federal University of São João del-Rei, MG, Brazil

15 <sup>5</sup>Center for Weather Forecast and Climatic Studies (CPTEC), Brazil

16 <sup>6</sup>National Oceanic and Atmospheric Administration Chemical Sciences  
17 Laboratory, Boulder, CO

18 <sup>7</sup>Department of Chemistry, Colgate University, Hamilton, NY

19 <sup>8</sup>Now at Ball Aerospace, Boulder, CO

20 <sup>9</sup>National Aeronautics and Space Administration (NASA) Langley Research  
21 Center, Hampton, VA

22 <sup>10</sup>Department of Chemistry, University of Colorado Boulder, Boulder, CO

23

24

25

26 \*Correspondence to Aditya Kumar ([akumar98@wisc.edu](mailto:akumar98@wisc.edu))

27

28

## 29 **Abstract**

30 We use the Weather Research and Forecasting with Chemistry (WRF-Chem) model with new  
31 implementations of GOES-16 fire radiative power (FRP) based wildfire emissions and plume-rise  
32 to interpret aerosol observations during the 2019 NASA-NOAA FIREX-AQ field campaign and  
33 perform model evaluations. We compare simulated aerosol concentrations and optical properties  
34 against observations of black carbon aerosol from the NOAA Single Particle Soot Photometer  
35 (NOAA-SP2), organic aerosol from the CU High Resolution Aerosol Mass Spectrometer (HR-  
36 AMS) and aerosol backscatter coefficients from the High Spectral Resolution Lidar (HSRL)  
37 system. This study focuses on the Williams Flats fire in Washington, which was repeatedly  
38 sampled during four science flights by the NASA DC-8 (August 3 – August 8, 2019). The  
39 emissions and plume-rise methodologies are implemented following NOAA’s operational High  
40 Resolution Rapid Refresh coupled with Smoke (HRRR-Smoke) forecasting model. In addition,  
41 new GOES-16 FRP based diurnal cycle functions are developed and incorporated in WRF-Chem.  
42 The FIREX-AQ observations represented a diverse set of sampled environments ranging from  
43 fresh/aged smoke from the Williams Flats fire to remnants of plumes transported over long  
44 distances. The Williams Flats fire resulted in significant aerosol enhancements during August 3-  
45 8, 2019, which were substantially underestimated by the standard version of WRF-Chem. The  
46 simulated BC and OC concentrations increased between 92 – 125 times (BC) and 28-78 times  
47 (OC) with the new implementation compared to the standard WRF-Chem version. These increases  
48 resulted in better agreement with the FIREX-AQ airborne observations for BC and OC  
49 concentrations (particularly for fresh smoke sampling phases) and aerosol backscatter coefficients.  
50 The model still showed a low bias in simulating the aerosol loadings observed in aged plumes  
51 from Williams Flats. WRF-Chem with the FRP-based plumerise simulated similar plume heights

52 to the standard plumerise model in WRF-Chem. The simulated plume heights (for both versions)  
53 compared well with estimated plume heights using the HSRL measurements. Therefore, the better  
54 agreement with observations ~~the improvements in the model simulation~~ were mainly driven by the  
55 higher emissions in the FRP-based version. The model evaluations also highlighted the importance  
56 of accurately accounting for the wildfire diurnal cycle and including adequate representation of  
57 the underlying chemical mechanisms, both of which could significantly impact model forecasting  
58 performance.

59  
60  
61  
62  
63  
64  
65  
66  
67  
68  
69  
70  
71  
72  
73  
74  
75  
76  
77  
78

79 **1. Introduction**

80 Wildfires are episodic ecosystem disturbances that play a key role in shaping and overall  
81 functioning of terrestrial ecosystems (Bond et al., 2005;Pausas and Ribeiro, 2017) and provide  
82 several ecosystem services (Pausas and Keeley, 2019). They also emit large amounts of pollutants  
83 into the atmosphere which can have important implications for air quality (McClure and Jaffe,  
84 2018;Jaffe et al., 2020), atmospheric chemistry/composition (Xu et al., 2021), human health (Xu  
85 et al., 2020), and the Earth’s radiation budget (Jiang et al., 2020). A particular concern associated  
86 with wildfire events arises from the serious health effects wildfire smoke can have (e.g. (Reid et  
87 al., 2016)). Wildfire regimes (e.g., frequency, size, and severity) have altered significantly over  
88 the past few years in the United States (US) with climate change hypothesized to be a major driving  
89 force (Flannigan et al., 2000;Holden et al., 2018;Halofsky et al., 2020). These alterations have  
90 been predicted to continue in the coming decades (e.g., Pechony and Shindell (2010)) resulting in  
91 growing concerns over the potential health impacts. In addition, long-range transport of smoke is  
92 a cause of concern for downwind communities.

93 Air quality forecasts generated by computational models are useful to assess the impacts a wildfire  
94 event could have on air quality (in the vicinity of the fire as well as at far away locations) and  
95 consequently the risk posed on human health due to smoke exposure. Thus, the accuracy of air  
96 quality forecasts both during fire events and in general is of paramount importance as highlighted  
97 by previous studies (e.g., Kumar et al. (2018);Al-Saadi et al. (2005)). Computational models used  
98 to provide air quality forecasts rely on a continuous ingestion of fire detections and properties  
99 available from either polar-orbiting or geostationary satellites and are run with the latest available  
100 information to generate smoke forecasts for the next few days (typically 36 to 72 hours). There are

101 several forecasting systems that have these models as a basis. Recently, Ye et al. (2021) have  
102 discussed and evaluated these forecasting systems during the **Fire Influence on Regional to Global**  
103 **Environment and Air Quality (FIREX-AQ)** field campaign in detail. The ability of computational  
104 models to accurately simulate air quality impacts during wildfire events is critically dependent on  
105 the inputs such as the estimated emissions, the simulated altitude of the emissions (smoke injection  
106 height, or plume-rise) (Val Martin et al., 2012;Carter et al., 2020) and meteorological variables  
107 (e.g., wind direction).

108 Wildfire emissions in the past have primarily been estimated following the model of Seiler and  
109 Crutzen (1980). There have been several fire emission inventories compiled over the years which  
110 use this methodology as the fundamental basis (e.g., **Global Fire Emissions Database (GFED)**  
111 (Van Der Werf et al., 2004;2006;2010;2017), **Fire INventory from the National Center for**  
112 **Atmospheric Research (FINN)** (Wiedinmyer et al., 2011)). However, this method is prone to  
113 uncertainties given the large number of parameters involved (burned area estimates, available  
114 biomass density, combustion efficiencies). Significant advances have been made in estimating the  
115 burned area with refined global estimates available. However, the uncertainties associated with  
116 available biomass density (ABD) and combustion efficiency estimates are particularly large and  
117 persist (e.g., (Reid et al., 2009)). An alternative emissions estimation approach is based on using  
118 the remote-sensing measurements of fire radiative power (FRP) and has formed the basis of  
119 multiple recent emission inventories (e.g., **Global Fire Assimilation System (GFAS)** (Kaiser et al.,  
120 2012), **Quick Fire Emissions Dataset (QFED)** (Darmenov and da Silva, 2015)). A major advantage  
121 FRP based approaches like GFAS provide is the ability to leverage key relationships, e.g., land  
122 cover specific consumption rates, from more comprehensive biogeochemical datasets like GFED  
123 in near-real time.~~The major advantage of this approach is a more direct estimation of fire emissions~~

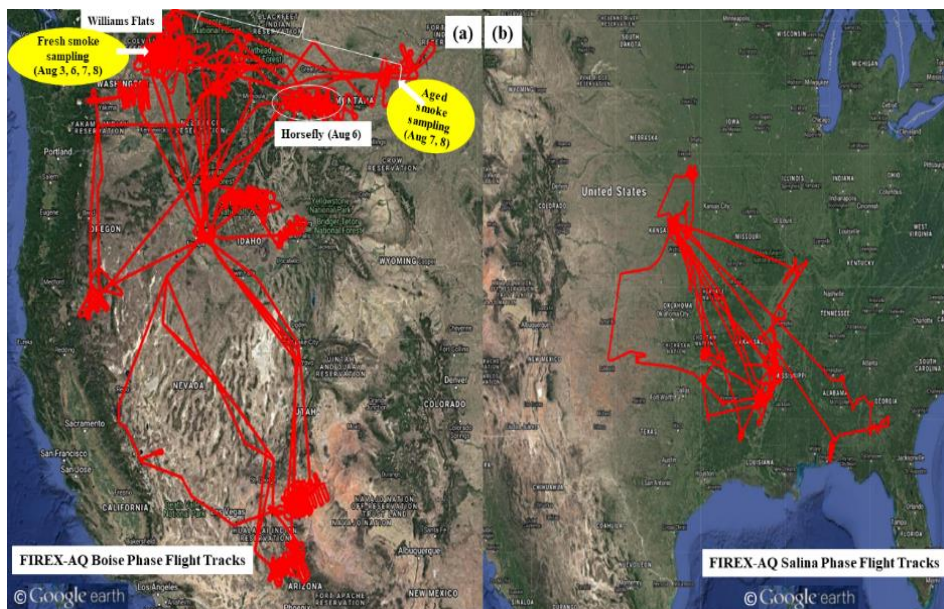
124 ~~without the need to use a multitude of parameters.~~ In addition, Wiggins et al. (2020) found  
125 significant correlations between GOES-16 FRP and in-situ measurements of important smoke  
126 tracers (e.g., CO<sub>2</sub>, CO). Wiggins et al. (2021) discuss in detail the differences in the two approaches  
127 to estimate fire emissions and the underlying uncertainties.

128 In contrast to fire emission inventories, the issue of estimating plume-rise in computational models  
129 has received considerably less attention. There have been a few plume rise approaches developed  
130 in the past with a detailed list provided by Val Martin et al. (2012). The approach developed by  
131 Freitas et al. (2007) (updates in Freitas et al. (2010)) has been the most commonly used. It has been  
132 evaluated by past studies (e.g., (Val Martin et al., 2012)) and has been embedded in several  
133 computational models including the **Weather Research and Forecasting with Chemistry (WRF-**  
134 **Chem)** model (described in Section 2). In recent work, a modified version of this approach has  
135 been included in the **High- Resolution Rapid Refresh coupled with Smoke (HRRR-Smoke)**  
136 **forecasting model** (described in Section 3) run operationally at the **National Oceanic and**  
137 **Atmospheric Administration (NOAA)**. The modified plume-rise approach incorporates FRP in  
138 computing the plume-rise. HRRR-Smoke also includes an FRP-based approach to estimate fire  
139 emissions. However, the HRRR-Smoke FRP-based approaches of estimating emissions and  
140 plume-rise together with GOES-16 FRP measurements have not been implemented in other  
141 computational models and no previous studies exist focusing on field observations based  
142 evaluation of the performance in WRF-Chem.

143 The 2019 FIREX-AQ field campaign (Roberts et al., 2018) was jointly led by the **National**  
144 **Aeronautics Space Administration (NASA)** and NOAA. The campaign took place during July –  
145 September 2019 in two phases. The first phase was held out of Boise (ID) (Figure 1 (a)) in the  
146 Western US ((July – August 2019) referred to as phase 1 hereon) and the second phase was out of

147 Salina (KS) (Figure 1(b)) ((August – September 2019) referred to as phase 2 hereon) in the South-  
148 Eastern US.

149



150  
151 **Figure 1: NASA DC-8 flight tracks during the Boise phase (a, left) and Salina phase (b, right)**  
152 **of the 2019 FIREX-AQ field campaign. The locations of Williams Flats fire and Horsefly fire**  
153 **which are the main focus of this study are shown (in white) along with the sampling dates**  
154 **and details. Image: Google Earth**

155

156 Phase 1 focused on wildfires primarily in the Western U.S. while Phase 2 was aimed at sampling  
157 agricultural (and prescribed) fires in the South-Eastern U.S. The campaign included a suite of  
158 measurement platforms aimed at sampling fire smoke at different altitudes and different times of  
159 the day. The goal of the campaign was to improve the current scientific understanding of fire  
160 behavior, fire smoke chemistry and its impact on atmospheric composition and air quality.  
161 Multiple airborne (NASA DC-8, NASA ER-2, NOAA CHEM-Twin Otter, and NOAA MET-Twin

162 Otter) and ground based measurement platforms were employed during the campaign to get a  
163 comprehensive sampling of the fires of interest. Mobile ground-based platforms (e.g., Aerodyne,  
164 NASA Langley Mobile Laboratory) provided high resolution ground level sampling of fire smoke.  
165 Wildfires occurring in different ecosystems and meteorological conditions and agricultural fires  
166 involving burning of different crop types were sampled using a suite of instruments aboard the  
167 different aircrafts. High temporal resolution measurements (typically 1 Hz, up to 20 Hz for some  
168 sensors) of important trace gas species (e.g., CO, O<sub>3</sub>, NO<sub>x</sub>, and VOCs) and aerosols (e.g., BC, OC)  
169 were carried out aboard the different aircraft. High Spectral Resolution Lidar (HSRL)  
170 measurements of aerosol optical properties are also available for all DC-8 flights of the campaign.

171 This study uses the WRF-Chem model with FRP-based fire emissions and plume-rise estimation  
172 methodologies employed in the HRRR-Smoke forecasting system to interpret aerosol observations  
173 during the FIREX-AQ field campaign and perform evaluations of retrospective aerosol forecasts  
174 with in-situ measurements available from the FIREX-AQ field campaign. Section 2 of this paper  
175 provides a general overview of the modeling tools including the WRF-Chem ~~model together with~~  
176 ~~details about the specific version being run at the University of Wisconsin Madison Space Science~~  
177 ~~and Engineering Center (UW Madison SSEC)~~ and the HRRR-Smoke models. Section 3 describes  
178 the data products used in this study including the GOES-16 fire product and in-situ measurement  
179 data available from FIREX-AQ. Section 4 presents discussion/interpretation of the FIREX-AQ  
180 observations and results from the model evaluation for the respective FIREX-AQ DC-8 science  
181 flights.

182

183



## 184 **2. Methodology**

### 185 **2.1. The WRF-Chem model**

186 The WRF-Chem model (Grell et al., 2005) is a model of meteorology, atmospheric  
187 chemistry/physics, and transport. It builds on the existing WRF model (Skamarock et al.,  
188 2019; Powers et al., 2017), which is primarily a weather forecasting model, by including full  
189 coupling of the meteorological component with a chemistry component. WRF-Chem uses the  
190 **Advanced Research WRF (ARW)** dynamical core to solve the flux-form of the non-hydrostatic  
191 Euler equations. It uses the Arakawa Staggered C-Grid horizontally whereas the vertical levels in  
192 the model are defined using a terrain following sigma-hybrid coordinate system (Skamarock et al.,  
193 2019) [\[Section 3.2 and Section 1.2\]](#). [\(Arakawa and Lamb, 1977\)](#). The **WRF Preprocessing System**  
194 (WPS) is the input pre-processing component of WRF-Chem. It is used to pre-process the  
195 terrestrial (e.g., 2-D vegetation, soil data) and meteorological (e.g., 3-D temperature, pressure  
196 fields) data to be compatible with the WRF-Chem configuration (model domain extent, grid size  
197 etc.). The chemistry component includes emissions of atmospheric species (anthropogenic,  
198 biogenic, geogenic (dust and volcanoes), fires), chemical mechanisms for gas-phase species and  
199 aerosols and atmospheric loss processes. Each chemical mechanism can either be coupled with  
200 aerosol schemes or run by itself. Dry deposition parameterization in the model follows the  
201 resistance-based scheme of Wesely (1989). The model supports both 1-way and 2-way horizontal  
202 nesting. WRF-Chem includes several schemes for microphysics (e.g., WRF Single-Moment 3-  
203 Class (WSM3) [\(Hong et al., 2004\)](#), Thompson [\(Thompson et al., 2004;2008\)](#) etc.), surface layer  
204 [\(e.g. Revised MM5 similarity theory \(Jiménez et al., 2012\), deep/shallow cumulus](#)  
205 [parameterization \(e.g., Grell-Freitas scheme \(Grell and Freitas, 2014\), GRIMs scheme \(Hong and](#)

206 Jang, 2018)), [land surface \(e.g. NOAH land surface model \(Chen and Dudhia, 2001\), planetary](#)  
207 [boundary layer \(e.g. Yonsei University PBL scheme \(Hong et al., 2006\), and atmospheric](#)  
208 [radiation \(e.g. Rapid Radiative Transfer Model for GCMs \(RRTMG scheme\) \(Iacono et al.,](#)  
209 [2008\)\)](#).

210 We use the WRF-Chem version run in real-time at the University of Wisconsin Madison [Space](#)  
211 [Science and Engineering Center](#) (WRFv3.5.1 and referred to as WRF-Chem hereon). It is a 1-way  
212 nested version of WRF-Chem and comprises of a regional domain spanning the continental United  
213 States (CONUS) with a horizontal spatial resolution of 8 km and 34 vertical layers (Greenwald et  
214 al., 2016). This model is used to provide daily chemical forecasts (currently for aerosols only) over  
215 CONUS and was one of the participating models providing chemical forecasting assistance for  
216 flight planning during FIREX-AQ. It uses the **Goddard Chemistry Aerosol Radiation and**  
217 **Transport/Georgia Tech-Goddard Global Ozone Chemistry Aerosol Radiation and Transport**  
218 (GOCART) mechanism to simulate tropospheric aerosol components (Chin et al.,  
219 2000a;2000b;2002;Ginoux et al., 2001). The simulated aerosol components include sulfate ( $\text{SO}_4^{2-}$   
220 ), hydrophilic and hydrophobic organic (OC) and black carbon (BC), dust, and sea-salt (SS) with  
221 no secondary organic aerosol (SOA) formation. No size distributions are included for  $\text{SO}_4^{2-}$ , OC  
222 and BC while a sectional scheme is used for dust (0.5, 1.4, 2.4, 4.5, 8.0  $\mu\text{m}$  and SS (0.3, 1.0, 3.2,  
223 7.5  $\mu\text{m}$ ). GOCART uses an [organic aerosol \(OA\)/OC ratio of 1.8](#), which is generally appropriate  
224 for fresh biomass burning organic aerosol emissions (Andreae, 2019) but low for more aged  
225 aerosol (Hodzic et al., 2020). The ~~a~~**Aerosol Optical-optical Depth-depth** (AOD) in the model is  
226 calculated at 550 nm by vertical integration of the aerosol extinction [using Mie scattering based](#)  
227 [look-up tables of effective radius and extinction coefficients as a function of relative humidity](#).  
228 Hygroscopic growth is accounted for [by determining hygroscopic growth factors from look-up](#)

229 tables computed using Mie theory following Martin et al. (2003) and extinction efficiencies are  
230 used as a function of mole fraction. The microphysics scheme is from Thompson et al. (2004), a  
231 modified version of the Rapid Radiative Transfer Model radiative scheme (RRTMG) is used for  
232 both shortwave (RRTMG\_SW) and longwave (RRTMG\_LW) radiation along with the Noah Land  
233 Surface Model (Noah-LSM) and the Mellor-Yamada-Janjic (Eta) surface layer scheme (Janjic,  
234 1996;2002).

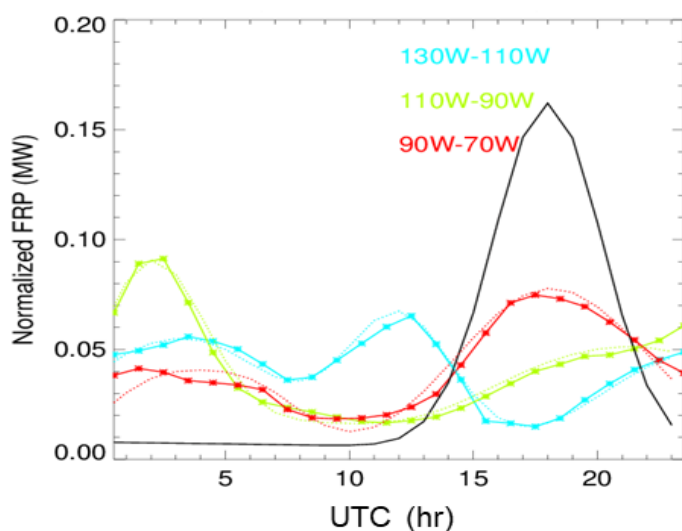
235 The initial (ICs) and lateral boundary conditions (LBCs) for meteorology and aerosol species (SO<sub>2</sub>,  
236 SO<sub>4</sub><sup>2-</sup>, Dimethyl sulfide (DMS), BC, OC, dust, SS) are from the Global Forecast System (GFS) and  
237 the global component of the Realtime Air Quality Modeling System (referred to as RAQMS  
238 hereon) (Pierce et al., 2003;2007;Natarajan et al., 2012) respectively. RAQMS combines chemical  
239 modeling and assimilation to provide 4-day global chemical forecasts. The version providing  
240 chemical ICs/LBCs for this study uses the GOCART mechanism, fire detections from MODIS,  
241 has a spatial resolution of 1° x 1° and the University of Wisconsin (UW) hybrid isentropic  
242 coordinate model as the dynamical core (Schaack et al., 2004). It has 35 vertical levels extending  
243 from the surface to the upper stratosphere (terrain-following at the surface to isentropic in the  
244 stratosphere). The modeling system is initialized with assimilation of total column ozone from the  
245 Ozone Monitoring Instrument (OMI), ozone profiles from MLS and AOD from MODIS. It also  
246 includes comprehensive stratospheric and tropospheric chemistry mechanisms (Pierce et al.,  
247 2007), which have been extensively evaluated (Kiley et al., 2003;Fairlie et al., 2007;Pierce et al.,  
248 2009;Al-Saadi et al., 2008;Natarajan et al., 2012;Yates et al., 2013;Sullivan et al., 2015;Baylon et  
249 al., 2016;Huang et al., 2017).

250 WRF-Chem employs the PREP-Chem (v1.3) emissions preprocessor (Freitas et al., 2011) to  
251 compute daily emissions of atmospheric species. These emissions include anthropogenic, fires,

252 volcanic, and biogenic sources, which are input to WRF-Chem at the start of a simulation. Fire  
253 emissions are based on the Brazilian Biomass Burning Emission Model (3BEM) (Longo et al.,  
254 2010), which is a fire burned area based bottom-up approach. The original version of the model  
255 was designed to use remote-sensing observations from both geostationary and polar-orbiting  
256 satellites. The geostationary satellite data was from the GOES WF\_ABBA product which included  
257 the instantaneous fire size whereas for polar orbiting satellites a mean fire size was assumed. The  
258 details of this approach are provided in Freitas et al. (2011). 3BEM computes daily emissions for  
259 110 species for each fire location. PREP-Chem at UW Madison has been modified to use only the  
260 GOES-16 Fire Detection and Characterization (FDC) product (described in Section 3.1). The  
261 GOES-16 FDC algorithm is an extension of the GOES Wildfire Automated Biomass Burning  
262 Algorithm (Section 3.1). Aboveground carbon density estimates are based on Olson et al. (2000)  
263 with later updates by (Gibbs, 2006;2007). The land cover data (Belward, 1996;Sestini et al., 2003)  
264 has a 1 km spatial resolution and 17 land cover types based on the International Geosphere-  
265 Biosphere Program (IGBP) land cover classification. Combustion factors and emission factors are  
266 based on look up tables. Emission factors are from Andreae and Merlet (2001) and Longo et al.  
267 (2009). The plume-rise model (Freitas et al., 2007;2010) is embedded in WRF-Chem and is a 1-  
268 D time-dependent entrainment plume model. This model is used to simulate the vertical  
269 distribution of emissions/plumerise for each WRF-Chem grid cell with a fire. It takes as input the  
270 emissions for the grid cell, fire properties (e.g., fire size), and other parameters (e.g., meteorology,  
271 land cover). The model provides as output the lower and upper levels between which the emissions  
272 are to be distributed. PREP-Chem computes daily emissions for each fire location, aggregates them  
273 on the 8km x 8km WRF-Chem grid and provides them as input (together with fire properties (e.g.,  
274 fire size)) for WRF-Chem and its plumerise model, which distributes the emissions in the vertical

275 domain. The diurnal cycle of wildfire emissions is simulated by using an analytical function which  
276 peaks at 18Z (Figure 2 (black curve)). This is the default diurnal cycle available with WRF-Chem  
277 and was developed based on fires in the Amazon (Freitas et al., 2011).

278 In operational/forecast mode, the model provides a 60-hour forecast every day. The forecast runs  
279 are initialized at 0000 UTC and use fire detection and meteorology data from the previous day.  
280 Fires are assumed to persist throughout the forecasting period. For this study, WRF-Chem was run  
281 for 36-hour periods in retrospective mode with a specific focus on the Boise phase of the FIREX-  
282 AQ field campaign.



283  
284 **Figure 2: The diurnal cycle functions (solid lines (green, blue, and red)) developed based on**  
285 **GOES-16 FRP data during the FIREX-AQ period. The original WRF-Chem diurnal cycle**  
286 **function is also shown (solid black line). The dashed lines (green, blue, and red) show the**  
287 **normalized FRP.**

288 In retrospective mode, the model has the same configuration as the forecast mode except that fire  
289 detections are for the current day, [and the NOAA National Center for Environmental Prediction](#)

290 (NCEP) Global Data Assimilation System (GDAS) (Wang and Lei, 2014) is used for and  
291 initial ~~lateral~~ and lateral boundary meteorological conditions and RAQMS is used for initial and  
292 lateral boundary aerosol conditions are from analyses. The modeling experiments consisted of two  
293 sets of simulations with different WRF-Chem versions. Set 1 included the WRF-Chem version  
294 with the default PREP-Chem v1.3 fire emissions estimates, the Freitas et al. (2007) plumerise  
295 model described earlier in this section (referred to as the 3BEM version hereon), and the diurnal  
296 cycle function peaking at 18Z. Set 2 included the version with fire radiative power (FRP) based  
297 emissions estimates and plumerise model (referred to as FRP version hereon). Both Set 1 and Set  
298 2 runs use the same emission factors from Andreae and Merlet (2001) and Longo et al. (2009).  
299 The FRP based updates are implemented following the **H**igh **R**esolution **R**apid **R**efresh **S**moke  
300 (HRRR-Smoke) modeling system which is a forecasting modeling system providing high temporal  
301 and spatial resolution (3 km) smoke forecasts for CONUS (using the VIIRS fire product)  
302 (described in the next section). We also developed new diurnal cycle functions (solid red, blue,  
303 and green curves in Figure 2) by adapting the default analytical function (shown in black in Figure  
304 2) to match the mean diurnal GOES-16 FRP profiles within three different longitude bands over  
305 the FIREX-AQ period (August-September 2019). The default diurnal cycle function for biomass  
306 burning emissions in WRF-Chem is a Gaussian function peaking at 18UTC (Freitas et al 2011).  
307 The GOES-16 FRP measurements during the FIREX-AQ period (August – September 2019) were  
308 divided into three zones based on longitude (zone 1 (blue in Figure 2): -130W to -110W, zone 2  
309 (green in Figure 2): -110W to -90W and zone 3 (red in Figure 2): -90W to -70W) and the mean  
310 FRP diurnal profiles were constructed for each zone. The default diurnal cycle function used in  
311 WRF-Chem was iteratively adjusted to match the FRP profiles for each zone resulting in three  
312 diurnal cycle functions. These diurnal functions were used in the FRP version.

### 313 **2.3. HRRR-Smoke model**

314 The High Resolution Rapid Refresh Smoke (HRRR-Smoke) model is a 3-D forecasting model  
315 (<https://rapidrefresh.noaa.gov/hrrr/HRRRsmoke/>), which is run at NOAA/NCEP. It uses a single  
316 smoke tracer to simulate smoke emissions and transport at a high spatial and temporal resolution  
317 to provide real-time smoke forecasts. The model domain spans the CONUS with a horizontal  
318 spatial resolution of 3 km and 50 vertical levels. HRRR-Smoke forecasts are initialized every hour  
319 using the HRRR meteorological analyses with the forecast lead times varying between 18-48  
320 hours. HRRR-Smoke is a coupled model where the direct radiative effects of smoke feedback on  
321 the dynamics. The model uses fire location (latitude, longitude) and FRP measurements from 4  
322 polar orbiting satellites, 2 ([Suomi-NPP and NOAA-20](#)) for VIIRS (375m resolution I-band Active  
323 Fire (AF) algorithm which is based on the Moderate Resolution Imaging Spectroradiometer  
324 (MODIS) Collection 6 retrieval (Giglio et al., 2016)) and 2 ([Terra and Aqua](#)) for MODIS. It  
325 employs an FRP based methodology to estimate fire smoke emissions and simulate plume-rise in  
326 the model. Smoke emissions in HRRR-Smoke are estimated by using FRP measurements to derive  
327 the fire radiative energy (FRE) over the fire duration (Ahmadov et al., 2017). The biomass burned  
328 is estimated by multiplying the FRE estimates with conversion coefficients from Kaiser et al.  
329 (2012). The model accounts for variation in these coefficients across ecosystems by using  
330 ecosystem specific conversion coefficients. The land cover types in HRRR-Smoke are defined  
331 following the IGBP land cover classification (17 land cover types). The plume-rise in the model  
332 is based on Freitas et al. (2007) with heat energy flux estimation parameterized as a function of  
333 FRP per unit fire size. HRRR-Smoke forecasts and simulations have been comprehensively  
334 evaluated for several fire seasons. These evaluations have included comparisons with hourly PM<sub>2.5</sub>  
335 measurements from the U.S. EPA Air Quality System Network at multiple sites in the Washington

336 state during the 2015 fire season (Deanes et al., 2016). The HRRR-Smoke model forecasts for  
337 FIREX-AQ were evaluated by Ye et al. (2021) using aircraft in-situ and remote sensing  
338 measurements.

### 339 **3. Data**

#### 340 **3.1. GOES-16 Fire Product**

341 GOES-16/GOES-East was the first in NOAA's GOES-R series of geostationary satellites. It was  
342 launched in November 2016 and occupies an orbit over 75.2°W. The **A**dvanced **B**aseline **I**mager  
343 (ABI) is a 16-channel (2 visible, 4 near-infrared, 10 infrared) passive imaging radiometer onboard  
344 GOES-16. It provides imagery of the Earth's surface and the atmosphere at very high spatial (2  
345 km for infrared bands) and temporal (5 min for CONUS, 15 min for the Western Hemisphere/Full-  
346 Disk) resolutions and includes several features that can be used to improve fire detection and  
347 emissions estimation. For example, the finer spatial and temporal resolution of ABI data would  
348 enable detection of small and short-lived fires. Under clear sky conditions, the minimum detectable  
349 size of a fire (mean temperature: 800K) is estimated to be 0.004 km<sup>2</sup> at the sub-satellite point.  
350 Short-lived fires are often missed by polar-orbiting satellites due to their limited temporal  
351 coverage.

352 The **F**ire **D**etection and **C**haracterization (FDC) product is one of the multiple GOES-16 ABI  
353 derived baseline products. The product has a spatial resolution of 2 km and is available for CONUS  
354 every 5 minutes. It uses a modified version of the Wildfire Automated Biomass Burning Algorithm  
355 (WF-ABBA) (Prins and Menzel, 1992;1994;Prins et al., 1998;2001;Schmidt and Prins, 2003)  
356 developed specifically for the ABI (referred to as ABI algorithm hereon). The ABI algorithm  
357 primarily relies on retrievals in the 3.9 and 11.2 μm spectral bands (ABI channels 7 and 14) and



358 channel 2 (if available during daytime) to identify fires and derive sub-pixel fire properties in a  
359 two-step process consisting of identifying potential fires and subsequently filtering out false  
360 alarms. The algorithm uses several ABI (brightness temperatures/radiances (Channels 7 and 14  
361 required, Channels 2 and 15 are optional), solar geometry and ABI sensor quality 3BEM flags)  
362 and non-ABI datasets (Global land cover classification, land/sea/desert mask from MODIS 5  
363 collection, NCEP total precipitable water, MODIS global emissivity) in the process of deriving  
364 the final fire product. The product provides fire detection locations (latitude, longitude), fire  
365 properties (e.g., sub-pixel instantaneous fire size, fire radiative power, fire brightness temperature  
366 etc.) and a metadata mask classifying each detection into one of six categories (Code 10(30):  
367 Processed fire (sub-pixel fire size and temperature estimated), Code 11(31): Saturated fire pixel,  
368 Code 12(32): Cloud contaminated (partially cloudy/smoke), Code 13(33): High probability fire,  
369 Code 14 (34): Medium probability fire and Code 15(35): Low probability fire. The codes in  
370 parenthesis are used when the detection also passes a temporal filtering test). We only use Codes  
371 10(30) in this study due to the availability of both FRP and fire size estimates. The sub-pixel  
372 instantaneous fire size and temperature is estimated using the Dozier technique (Dozier, 1981).  
373 The Dozier method utilizes the total radiances in the 3.9 and 11.2  $\mu\text{m}$  spectral bands and the  
374 respective radiances in these bands from the fire and the background to solve for the proportion of  
375 each ABI pixel that is on fire. Under realistic conditions (likely to be encountered in an operational  
376 environment), Giglio and Kendall (2001) estimated that the random errors (at one standard  
377 deviation) in estimating the fire size could be within 50% when the proportion of the pixel on fire  
378 is more than 0.005. For proportions lower than 0.005, both the systematic and random errors could  
379 be greater. GOES-16 data for the FIREX-AQ campaign period was available publicly.

## 380 **3.2. NASA DC-8 Airborne Observations from FIREX-AQ**

381

### 382 **3.2.1. Black Carbon Measurements from the NOAA Single-Particle Soot Photometer (SP2)**

383 We use refractory Black Carbon (rBC) measurements from the NOAA Single Particle Soot  
384 Photometer (SP2) (Schwarz et al., 2006;2008;2010a;2017;Perring et al., 2017) to evaluate WRF-  
385 Chem simulated BC. Henceforth, we use the terminology BC to refer both to the material  
386 quantified by the SP2, and the modeled species. The SP2 is primarily used to measure the  
387 refractory Black Carbon (rBC) mass content of individual accumulation mode aerosol particles.  
388 These mass estimates are independent of the particle mixing state or morphology. The instrument  
389 has been used on various research aircrafts to provide airborne rBC in-situ measurements in  
390 multiple field campaigns (e.g., NASA DC-8 (SEAC4RS) (Perring et al., 2017), NSF/NCAR GV  
391 (HIPPO)(Schwarz et al., 2010b)). The SP2 flew onboard the NASA DC-8 for both the Boise and  
392 Salina phases of the FIREX-AQ field campaign and provided in-situ measurements of rBC mass  
393 concentration ( $\text{ng -BC/std. m}^3$ , (1013 mb pressure and 273K temperature) at 1-Hz frequency. The  
394 rBC concentrations reported by the SP2 include final calibrations and adjustments for dilutions, a  
395 correction factor to account for the non-detected rBC (sizes outside of SP2 detection range (90-  
396 550 nm)) as well as rejection of highly contaminated (due to high concentrations) observations.  
397 Smaller concentration biases also occurring under high aerosol loadings (Schwarz et al., under  
398 review 2021) but affecting rBC concentrations by well less than 20% have not been corrected.

399 ~~These biases are negligible in the context of the model comparison here. Total uncertainty in~~  
400 accumulation-mode rBC concentrations measured by the SP2 are  $\leq 40\%$  in FIREX-AQ. As  
401 GOCART does not resolve BC aerosol size, and most BB emissions occur in this size

402 [range, measurement bias relative to the model is negligible in the context of the ~order of](#)  
403 [magnitude shifts arising from emissions treatments explored here.](#)

### 404 **3.2.2. Organic Aerosol Measurements from the University of Colorado Boulder Aircraft** 405 **High-Resolution Time-of-Flight Aerosol Mass Spectrometer**

406 We use ~~Organic Aerosol~~(OA) mass concentration measurements from The University of Colorado  
407 Boulder Aircraft High-Resolution Time-of-Flight Aerosol Mass Spectrometer (CU HR-ToF-  
408 AMS) and use the provided OA/OC ratio (based on (Aiken et al., 2008;Canagaratna et al., 2015))  
409 to derive OC concentrations for comparison to the WRF-Chem simulated OC concentrations  
410 (Note: OA/OC is not computed for OA values under the detection limit, and for those datapoints  
411 a value of 1.8 OA/OC was used, consistent with the GOCART assumptions). The CU HR-ToF-  
412 AMS (DeCarlo et al., 2006) can be used to perform high temporal resolution (demonstrated ability  
413 of measurements at 0.1 Hz (Guo et al. (in prep)) measurements of bulk organic aerosol with  
414 extensive characterization of its intensive properties (e.g., O/C, H/C, PMF factors) and inorganic  
415 salts (e.g., ammonium sulfate ((NH<sub>4</sub>)<sub>2</sub>SO<sub>4</sub>), nitrate (NH<sub>4</sub>NO<sub>3</sub>) and chloride (NH<sub>4</sub>Cl)) in submicron  
416 (up to 900 nm vacuum aerodynamic diameter (Guo et al., 2021)). It is one of the several available  
417 versions of the AMS that incorporates an improved high-resolution mass spectrometer. The  
418 instrument takes in ambient air through a dedicated aerosol inlet (HIMIL (Stith et al., 2009)) into  
419 an aerodynamic lens (residence time < 0.4 s) which directs the particles into a narrow beam. The  
420 non-refractory particles are subsequently vaporized by impaction on a heated surface (600 °C) and  
421 the vapors are ionized by electron ionization. Finally, these ions are analyzed by mass  
422 spectrometry. The CU HR-ToF-AMS flew onboard the NASA DC-8 for both the Boise and Salina  
423 phases of the FIREX-AQ field campaign. The instrument provided in-situ measurements at 1-Hz

424 frequency and switched to a higher time resolution of 5 Hz to sample fire plumes, especially the  
425 smaller ones in the Salina phase.

426 AMS organic carbon (OC) is estimated from the total OA mass concentration and OA/OC mass  
427 ratio measurements. OA/OC is derived from carefully fitting all the organic peaks in the mass  
428 spectrum and applying a calibration (Aiken et al., 2008). The uncertainty ( $2\sigma$ ) in OA is estimated  
429 as 38% (Bahreini et al., 2009), based on the uncertainty in the relative ionization efficiency  
430 (Jimenez et al., 2016; Xu et al., 2018) and AMS collection efficiency (Middlebrook et al., 2012).  
431 This uncertainty was shown to be consistent with AMS measurements of aged particles (Guo et  
432 al., 2021). OA/OC is estimated using two approaches: the “improved Aitken ambient” calibration  
433 for OA concentrations under  $150 \mu\text{gsm}^{-3}$  and the “Aitken semi-explicit method” for OA  
434 concentrations higher than this (so most of the plume data in this study), as described in  
435 Canagaratna et al. (2015). Based on that analysis, for complex mixtures the uncertainty in OA/OC  
436 is estimated at 8% ( $2\sigma$ ). Hence the total estimated uncertainty for OC is 39%.

### 437 **3.2.3. Aerosol Optical Property Measurements from the NASA Langley Airborne High** 438 **Spectral Resolution Lidar (HSRL)**

439 We use backscatter coefficient (532 nm) measurements from the NASA Langley airborne High  
440 Spectral Resolution Lidar (HSRL) (Hair et al., 2008) to compare to WRF-Chem simulated  
441 backscatter coefficient. WRF-Chem backscatter coefficient is computed using the ratio of the  
442 WRF-Chem simulated aerosol extinction coefficient for different species (BC+OC,  $\text{SO}_4^{2-}$ , dust,  
443 SS) and the corresponding lidar ratios. The lidar ratios are used from Burton et al. (2012). The  
444 HSRL can provide measurements of aerosol backscatter and extinction coefficients (532 nm),  
445 aerosol backscatter coefficient (1064 nm) and aerosol depolarization (532 nm and 1064 nm). The  
446 instrument employs the HSRL technique at 532 nm and the standard backscatter lidar technique at

447 1064 nm. The HSRL technique relies on the differences in the spectral distributions of the  
448 backscattered lidar signal from aerosols and molecules. The returned lidar signal is split into two  
449 optical channels, namely the molecular backscatter channel and the total backscatter channel. The  
450 molecular backscatter channel consists of an iodine (I<sub>2</sub>) vapor absorption filter, which removes the  
451 aerosol component of the returned lidar signal but passes the component due to molecules. The  
452 total backscatter channel is non-selective and allows all frequencies to pass. The uncertainties in  
453 the HSRL backscatter coefficient measurements (532 nm) can be mainly attributed to the iodine  
454 filter transmission measurements, calibration errors, molecular depolarization and atmospheric  
455 state variable measurements (Hair et al, 2008). The combined systematic error in the aerosol  
456 backscatter due to these factors is estimated to be less than 2.3% (Hair et al, 2008).

457

## 458 **4. Results and Discussion**

459

460 This section includes a discussion of the relevant FIREX-AQ flights, interpretation of the FIREX-  
461 AQ aerosol observations and evaluation of the WRF-Chem model (3BEM and FRP versions) using  
462 FIREX-AQ observations of BC and OC, backscatter ~~and also compares simulated plume heights~~  
463 ~~with observed plume heights from the HSRL data.~~ It also includes comparisons of simulated WRF-  
464 Chem AOD with observed AOD from GOES-16/17 and simulated plume heights with observed  
465 plume heights from the HSRL data. Plume height estimates are computed using the HSRL  
466 backscatter measurements and WRF-Chem simulated backscatter. Plume height is defined as the  
467 height at which the maximum change in the magnitude of the backscatter gradient is observed. We  
468 only focus on FIREX-AQ DC-8 science flights during August 3-7, 2019. We do not include the  
469 flight on August 8, 2019, in the analysis since the primary focus of this flight was on the ~~Pyro-Cb~~

470 Pyro-Cumulonimbus cloud (pyro-Cb) produced by Williams Flats and current computational  
471 models do not have the capability to simulate these events. The WRF-Chem plumerise (in both  
472 3BEM and FRP version) is a 1-D cloud model with a simplified microphysics scheme without any  
473 coupling between heat fluxes generated from fires and meteorology. Therefore, simulation of  
474 PyroCb-pyro-Cb events is beyond the capability of current computational models. Ye et al. 2021  
475 also reported the current inability of models to represent the simulate PyroCb-pyro-Cb events based  
476 on their analyses of multiple forecasting models. However, recent work has focused on conceptual  
477 models that describe PyroCb-pyro-Cb (e.g., Peterson et al. (2017)) development during wildfire  
478 events. These models could serve as a starting point towards incorporating PyroCb-pyro-Cb  
479 simulation capabilities in current computational models. ~~For each FIREX-AQ DC-8 science flight,~~  
480 ~~we first provide an overview of the flight followed by a qualitative comparison of the observations~~  
481 ~~with WRF-Chem using HSRL flight curtains and finally quantitative comparisons between~~  
482 ~~FIREX-AQ observations and WRF-Chem are discussed.~~ We first provide an overview of the  
483 Williams Flats fire (Section 4.1), followed by brief descriptions of each FIREX-AQ DC-8 science  
484 flight (Section 4.2). The subsequent sections provide an evaluation of the WRF-Chem simulated  
485 aerosol optical properties and BC/OC concentrations during each of the FIREX-AQ DC-8 science  
486 flights. All altitudes reported are with respect to mean sea level (msl). We use the aircraft pressure  
487 altitude to represent the aircraft altitude. The WRF-Chem Planetary Boundary Layer (PBL) height  
488 was converted to the msl reference by adding the surface height to the WRF-Chem PBL variable.

## 489 **~~4.1. BC and OC Emission Estimates~~**

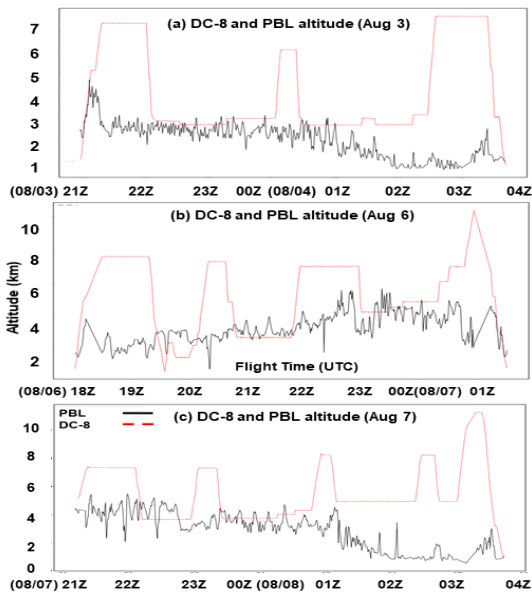
### 490 **4.1. The Williams Flats fire**

491 The Williams Flats wildfire began on August 2, 2019, 5 miles Southeast of Keller (Southwestern  
492 Ferry County) in Washington (WA) USA. The fire was caused by lightning strikes accompanying  
493 an early morning thunderstorm near the Colville Indian Reservation. The 100% containment date  
494 for the fire was reported to be August 25, 2019, and it burned an estimated 44,446 Acres (Source:  
495 Inciweb). The fire was the flagship fire of the Boise phase of the FIREX-AQ campaign and the  
496 focus of the DC8 science flights on August 3, 6, 7, and 8, 2019. These flights sampled both fresh  
497 and aged smoke plumes from the fire. On August 8, 2019, the fire also generated a pyro  
498 cumulonimbus cloud (PyroCb) pyro-Cb, which was sampled by the DC8 science flight for the day.  
499 The DC-8 science flight on August 6<sup>th</sup> also focused on the Horsefly fire. The Horsefly fire started  
500 on August 5, 2019, 15 miles east of Lincoln in the Lewis and Clark County (Montana) and burned  
501 1274 acres in the first 24 hours. The fire was reported to have burned 1350 acres till August 23,  
502 2019, with zero growth reported in the prior week.

503 ~~**4.2. Evaluation of WRF-Chem Simulations for DC-8 FIREX-AQ**~~  
504 ~~**Science Flights (August 3–7, 2019)**~~

505 **4.2. The FIREX-AQ DC-8 Science Flights (August 3-7, 2019)**

506



507

508 **Figure 3: The DC-8 flight altitude (red) and the WRF-Chem planetary boundary layer height**  
 509 **(black) for the August 3, 2019 (a), August 6 (b) and August 7 (c) flights**

510

#### 511 **4.2.1 August 3, 2019, Flight**

512

513 The FIREX-AQ DC-8 science flight on August 3<sup>rd</sup>, 2019, involved extensive sampling of the  
 514 Williams Flats fire and a high altitude remnant of smoke associated with long-range transport.

515 Figure 3 (a) shows the flight track along with the WRF-Chem simulated PBL. This science flight

516 started with the DC-8 flying over the Lick/Mica Creek fire on way from Boise to Williams Flats

517 (~ between 21:00Z and 21:30Z). The overall flight could be divided into two phases. Phase 1 (22Z

518 – 00Z) was carried out at altitudes ranging from 2.7 – 3 km and sampling of the smoke plume

519 extending 120 km downwind of the fire in the northeast direction. Between 21:30Z and 22:00Z,

520 the aircraft travelled across Williams Flats to begin phase 1 of sampling. Phase 2 (~ 00:30Z –



521 02:30Z) extended 65 km downwind of the fire, initially in the northeast direction and later in the  
522 eastern direction. The altitudes of sampling ranged between 3-3.4 km. Phase 2 began following a  
523 transit (between 00Z and 1Z) to the fire after phase 1.

#### 524 **4.2.2 August 6, 2019, Flight**

525

526 The FIREX-AQ DC-8 science flight for August 6<sup>th</sup>, 2019, had two targets namely, Williams Flats  
527 and the Horsefly fire in Montana (Figure 3 (b)). Williams Flats was sampled first followed by an  
528 extensive sampling of Horsefly which spanned more than 200 km downwind of the fire. For  
529 Williams Flats, the sampling could be divided into two phases with phase 1 focusing on sampling  
530 low elevation smoke and phase 2 involving sampling of the fire plume at a higher altitude (~3 km).  
531 Between 22Z-23Z, the DC-8 travelled from Williams Flats towards Montana to sample the  
532 Horsefly fire and flew over the Snow Creek fire and Horsefly before beginning the sampling. For  
533 the Horsefly fire, the DC-8 travelled downwind in the plume starting at ~23Z and continuing  
534 sometime after 00Z, which was followed by an upwind pass and return to Boise.

#### 535 **4.2.3 August 7, 2019, Flight**

536

537 The August 7<sup>th</sup>, 2019, FIREX-AQ DC-8 science flight (Figure 3(c)) focused exclusively on the  
538 Williams Flats fire with a four phase sampling strategy. Phase 1 involved sampling aged (transport  
539 age: one day old) smoke from the fire which was transported eastward to Montana. This smoke  
540 was sampled both in the East and West directions travelling along the axis of the plume. The  
541 remaining phases focused on fresh smoke from the fire with phase 2 involving sampling at low  
542 altitudes (~ 3.7 - 4.3 km) and phases 3 and 4 involved higher altitude (~ 4.9 km) sampling.

### 4.3. BC and OC Emission Estimates

Figure 4 shows the estimated BC and OC emissions (3BEM and FRP versions) for the Williams Flats fire on the DC-8 flight days (August 3- 8, 2019). Emissions from the Horsefly fire which was sampled on the August 6<sup>th</sup> flight are also shown. In general, the BC and OC emissions estimates from the FRP approach were significantly higher than the 3BEM approach on all flight days for the Williams Flats fire. For BC, the FRP-based emissions were 32 times higher on August 3<sup>rd</sup>, when Williams Flats was in its initial stages and varied between 12 to 47 times the emissions in the 3BEM version till August 8<sup>th</sup>, 2019.

Formatted: Superscript

Formatted: Superscript

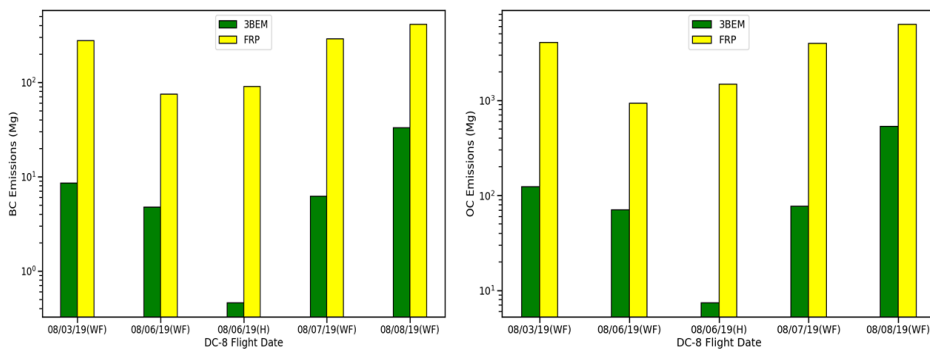


Figure 4: Model-predicted BC (a, top) and OC (b, bottom) emissions from the Williams Flats (WF) fire on the DC-8 science flight days (August 3 – 8 2019) during FIREX-AQ. The emissions for Horsefly (H) fire on August 6, 2019, are also included (Bar set 3 for BC and OC).

OC emissions also showed a similar trend with the FRP version emissions being 33 times higher on August 3<sup>rd</sup> and 12-52 times higher for the remaining flight days. BC and OC emissions for both approaches increased during August 3-8, with the maximum emissions observed on August 8<sup>th</sup>, 2019, when Williams Flats generated a PyroCb pyro-Cb event. The Williams Flats fire increased from 10,438 acres to 40,000 acres during August 3 -8 (source: *Inciweb August 4 and August 9, 9:00 am update*) which is reflected in the increase in BC and OC emissions. ~~The increases were~~

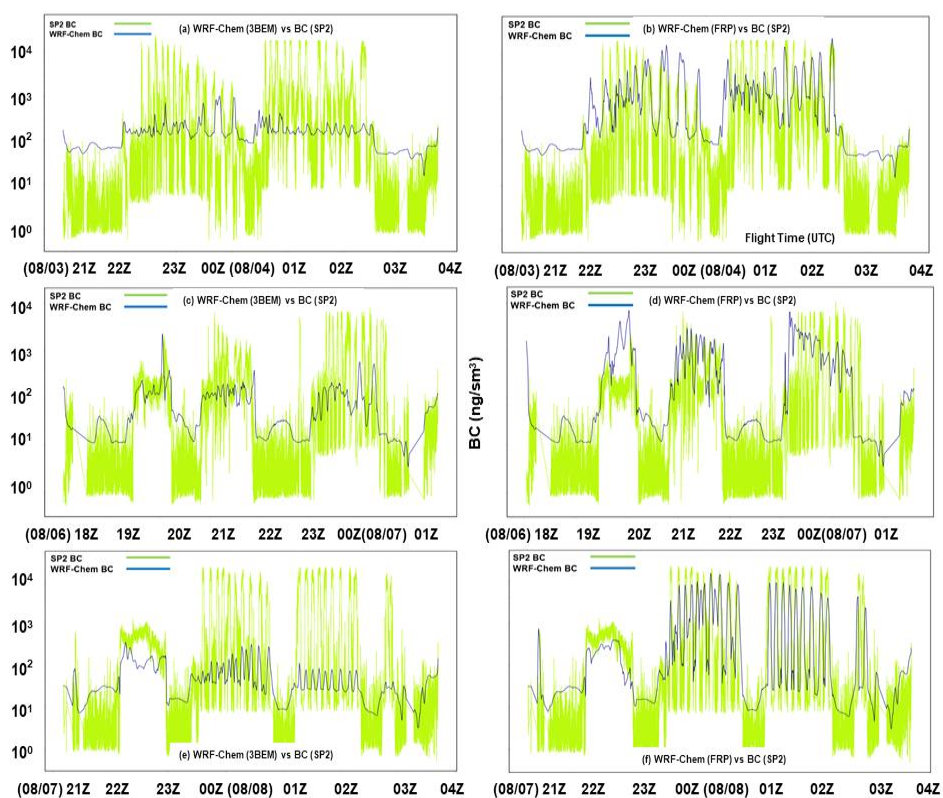
Formatted: Superscript

562 ~~much larger for the FRP based approach indicating that the FRP based methodology is more~~  
563 ~~sensitive to the changes in fire behavior over time.~~ Emissions in the 3BEM version were lower for  
564 the Horsefly fire as well with the FRP based emissions being 198 times higher for BC and 200  
565 times higher for OC. Thus, the FRP-based approach yielded substantially higher emissions from  
566 wildfires as compared to the 3BEM approach. The significant differences in emissions in the two  
567 approaches could be attributed to the fundamental difference in the emissions estimation  
568 methodology in the two approaches. The 3BEM approach uses the instantaneous fire size while  
569 the HRRR-Smoke approach uses the FRP. Both these parameters could vary at substantially  
570 different rates over the lifetime of a fire and therefore could lead to very different results. Ye et al.  
571 (2021) compared the emissions between 12 different forecasting systems including WRF-Chem  
572 at UW Madison (using GOES-15 fire product) and HRRR-Smoke and found that models using  
573 FRP-based emission estimation approaches had substantially (mean factor of 5.6) higher emissions  
574 than those using burned-area based (referred to as hotspot-based in their study) approaches.

575 We used the same emission factors in both the 3BEM and FRP versions to ensure that the changes  
576 in emissions solely represent the differences in the two methodologies. Considerable progress has  
577 been made in improving upon the emission factor estimates used in this study. For example,  
578 subsequent work by Akagi et al. 2011 (referred to as AK11), and Andreae 2019 (referred to as  
579 AN19) have resulted in new emission factor estimates for biomass burning. In comparison to these  
580 studies, our OC emission factors for tropical forests were 9% higher than AK11 (BC: 21%) and  
581 15% higher than AN19 (BC: 23%) while for extratropical forests the emission factors were the  
582 same as AK11. AN19 did not report emission factors for extratropical forests. For  
583 savanna/grasslands, OC emission factors were 18% higher than AK11 (BC: 20%) and 6% higher

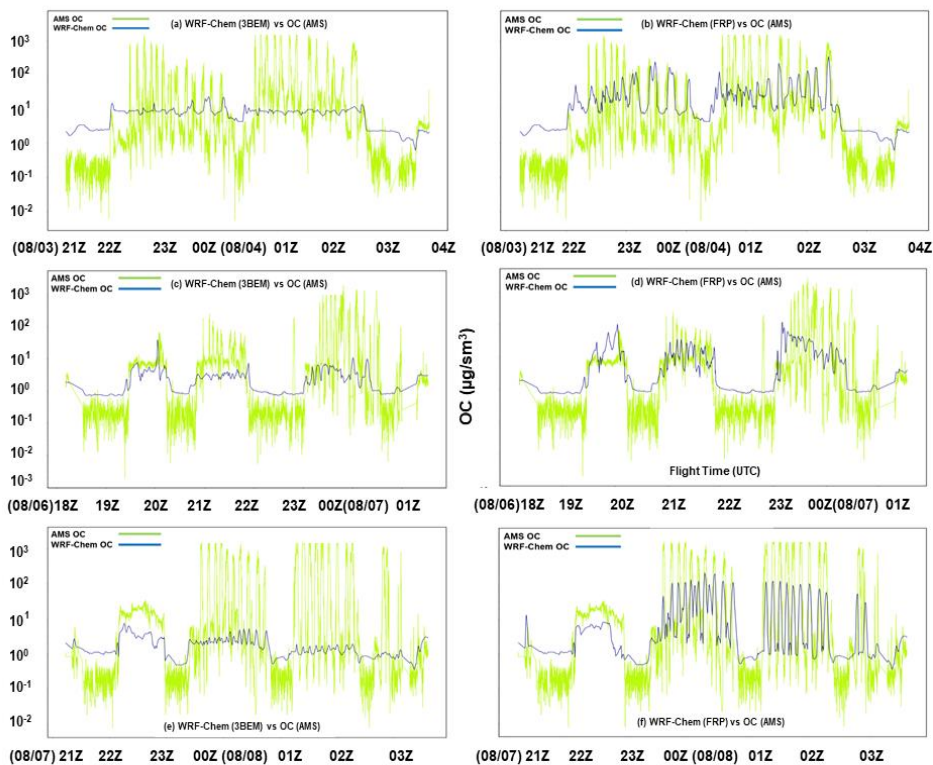
584 than AN19 (BC: 15%). Thus, incorporation of these emission factors could alter the magnitude of  
585 emission estimates (for both 3BEM and FRP versions) reported in Figure 4.

586 **4.4. Simulated Aerosol (BC and OC) Concentrations during the**  
587 **Williams Flats fire**



588  
589 **Figure 5: (a) Time series for BC (SP2) in-situ measurements and corresponding WRF-Chem**  
590 **simulated BC (3BEM and FRP versions) for the August 3 (a, b), August 6 (c, d) and August**  
591 **7 (e, f) DC-8 science flights OC (AMS) in-situ measurements and corresponding simulated**  
592 **OC (WRF-Chem 3BEM (d) and FRP (e)).**

593



594  
 595 **Figure 6: (a) Time series for OC (AMS) in-situ measurements and corresponding WRF-**  
 596 **Chem simulated BC (3BEM and FRP versions) for the August 3 (a, b), August 6 (c, d) and**  
 597 **August 7 (e, f) DC-8 science flights**

598  
 599 Figures 5 and 6 show the time series of in-situ measurements of BC (SP2) and OC (AMS) and the  
 600 WRF-Chem simulated BC and OC (3BEM and FRP) along the DC-8 flight track for the DC-8  
 601 science flights. For the August 3<sup>rd</sup> flight, the 3BEM version was up to a factor of 100 lower than  
 602 the in-situ BC measurements in phase 1 of sampling and up to ~ 250 times lower in phase 2 (Figure  
 603 5 (a)). For OC (Figure 6 (a)), the 3BEM version underestimated the measurements by up to ~ 125  
 604 times in phase 1 and up to more than 300 times in phase 2. Similar results were obtained for the

605 other flights as well, where the 3BEM version was biased low for most part of the August 6<sup>th</sup> flight  
606 with the simulated BC up to 440 times lower than the measurements (Figure 5(c)) and OC up to  
607 1065 times lower (Figure 6(c)), while for the August 7<sup>th</sup> flight, the 3BEM version was not able to  
608 reproduce the observed BC (Figure 5 (e)) and OC concentrations (Figure 6 (e)) during any of the  
609 sampling phases. The underestimations were up to 842 times for BC and up to 1439 times for OC.  
610 The 3BEM version performed particularly poorly in phases 3 and 4 of the flight where the low  
611 biases were very large ~~and could be caused by the low emissions in the later stages of the flight~~.  
612 These results can be attributed mainly to the low emissions in the 3BEM version. The greater  
613 underestimation in phase 2 for BC and OC (August 3<sup>rd</sup> flight) and phases 3 and 4 of the August 7<sup>th</sup>  
614 flight could be due to the diurnal cycle imposed on the emissions resulting in lower emissions  
615 during these stages of the respective flights.

616 The higher emissions in the FRP version result in better agreement with the SP2 and AMS in-situ  
617 measurements throughout the flight periods. During the August 3<sup>rd</sup> flight, the FRP version was  
618 able to reproduce the BC and OC enhancements observed near the fire and downwind well, with  
619 the simulated BC being up to a factor of ~ 91 higher than the 3BEM version (Figure 5(b)), while  
620 for OC (Figure 6(b)), the FRP version was up to ~28 times higher. Thus, the FRP version showed  
621 a significant reduction in discrepancies between WRF-Chem and the SP2/AMS in-situ  
622 measurements. During the August 6<sup>th</sup> flight as well, the FRP version showed very good agreement  
623 for phase 2 of the Williams Flats sampling, where it was able to simulate comparable  
624 concentrations of BC and OC to the observations (Figure 5(d), Figure 6(d)). For the Horsefly fire  
625 as well, the FRP version was able to simulate the high BC levels observed (Figure 5(d), 23Z  
626 onward) but significantly underestimated OC (Figure 6(d), 23Z onward). The FRP version  
627 simulated up to 125 times higher BC concentrations and up to 49 times higher OC concentrations

628 than the 3BEM version. The 3BEM version was biased very low for BC and OC during phase 2  
629 of Williams Flats and the Horsefly sampling. The BC and OC concentrations in the FRP version  
630 (Figure 5(d), Figure 6(d), 23Z onward) declined sharply as the DC-8 flew downwind of Horsefly,  
631 which could be attributed to an underestimation of the injection heights or inability of the model  
632 to accurately simulate the transport of the plume downwind resulting in lower plume heights than  
633 observed. The Horsefly fire plume altitude increased downwind as shown in the HSRL backscatter  
634 measurements (Figure 9(d), 23Z onward). This was accompanied by a gradual ascent of the DC-8  
635 aircraft as it tracked the fire plume (Figure 9(d)). Since the plume-height was very low in the  
636 model, the BC and OC concentrations along the flight track represented background level  
637 concentrations instead of the enhanced levels caused by the fire. These concentrations declined  
638 even further as the aircraft ascended in the later stages, which is observed in the time-series during  
639 the Horsefly downwind sampling phase. However, the FRP version performed poorly as compared  
640 to the 3BEM version in simulating the low elevation smoke as the FRP version significantly  
641 overestimated the BC and OC concentrations (Figure 5(d), 6(d), 19Z – 20Z). During the August  
642 7<sup>th</sup> flight as well, the FRP version was able to reproduce the observations very well especially in  
643 the fresh smoke sampling phases of the flight. The higher emissions in the FRP version resulted in  
644 BC concentrations up to 124 times higher and OC concentrations up to 78 times higher than the  
645 3BEM version (Figure 5(e, f) and Figure 6(e, f)). Both the 3BEM and FRP versions underestimated  
646 the aged smoke which could be due to simplified chemistry in the GOCART mechanism. The  
647 underestimation of OC in the model was larger than BC which could also be a consequence of the  
648 simplified chemistry in the model.

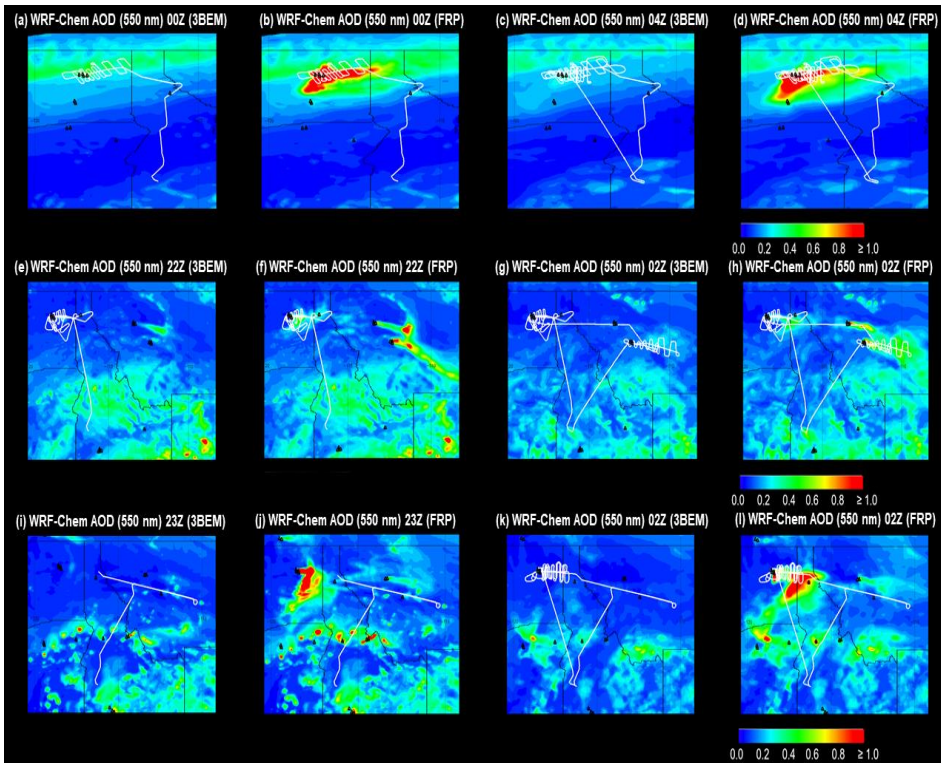
649

650

651 **4.5. Simulated Aerosol Optical Properties during Williams Flats**

652 **4.5.1. Aerosol Optical Depth (AOD)**

653



654

655 **Figure 7: WRF-Chem simulated aerosol optical depth (AOD) for the 3BEM and FRP**  
656 **versions during the FIREX-AO DC-8 science flights on August 3 (a-d), August 6(e-h) and**  
657 **August 7 (i-l). The DC-8 flight track is overlaid. The triangle markers indicate the locations**  
658 **of active fires.**

659

660



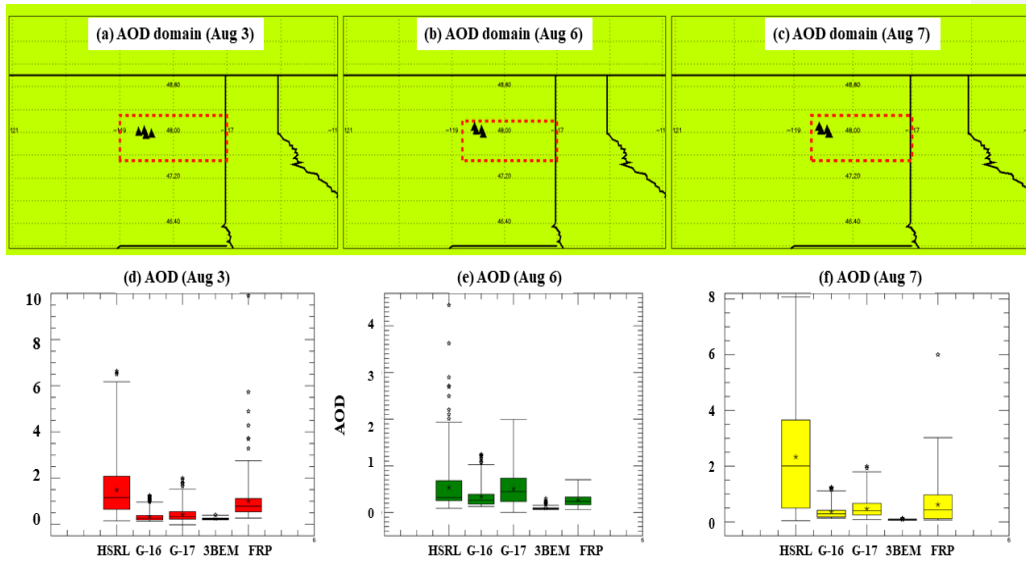
661 Figure 7 shows the WRF-Chem simulated AOD (3BEM and FRP versions) for the Williams Flats  
662 fire during the August 3<sup>rd</sup> (a-d), August 6<sup>th</sup> (e-h) and August 7<sup>th</sup> (i-l) DC-8 science flights. The  
663 DC-8 flight track during the different phases of each flight is overlaid. The 3BEM version  
664 simulated substantially low AOD enhancements during all the science flights as compared to the  
665 FRP version. During the August 3<sup>rd</sup> flight (Figure 7 (a, c)), minor AOD enhancements (~ 0.3-0.6)  
666 were simulated due to the Williams Flats fire. AOD enhancements were higher in the vicinity of  
667 the fire during phase 1 of sampling (Figure 7(a), 00Z)) but dissipated during the latter stages of the  
668 flight (Figure 7(c), 04Z, AOD: 0-0.2). For the remaining flights as well, the simulated AOD  
669 enhancements were very low (August 6<sup>th</sup> (0.0 – 0.3) and August 7<sup>th</sup> (0.2-0.6)) as compared to those  
670 in the FRP based version. The simulated plumes for the Williams Flats and Horsefly fires during  
671 the August 6<sup>th</sup> flight were either thin or not noticeable while for the August 7<sup>th</sup> flight, the AOD  
672 enhancements (0.2 - 0.6) were prominent only during the early stages of the flight and further  
673 declined during the fresh smoke sampling phase. The plume from the Williams Flats fire was only  
674 evident during the early stages of the flight and was characterized by very low aerosol loadings.  
675 In contrast, on August 3<sup>rd</sup>, the FRP version simulated significantly higher AOD enhancements both  
676 near the fire as well as in the transported plume downwind. These enhancements persisted  
677 throughout the DC-8 sampling period at 00Z and 04Z. On August 6<sup>th</sup>, the FRP version simulated  
678 well defined plumes with higher AOD (0.3- >=1.0) for both Williams Flats and Horsefly. The  
679 spatial location and extent of the plumes were in good agreement with the DC-8 sampling legs  
680 with the Horsefly fire plume being represented very well by this version (Figure 7 (h)) based on  
681 the DC-8 sampling pattern. Similar agreement was observed for the plume from Williams Flats  
682 which was predominantly towards the East. Similar results were obtained for the August 7<sup>th</sup> flight,  
683 with very high AOD enhancements (>=1) near the fire both before and during the fresh smoke

684 sampling phase and a well-defined and persistent plume throughout the DC-8 sampling period  
685 coincided well with the DC-8 flight path during the fresh smoke sampling phases. The aged smoke  
686 plume from Williams Flats in Montana did not appear as a distinct feature in the WRF-Chem AOD  
687 plots for both versions which could possibly be due to the low simulated aerosol concentrations.  
688 The lower AOD simulated by the 3BEM version is primarily due to the lower emissions (Section  
689 4.3) in comparison to the FRP version while the decline in AOD during phase 2 (August 3<sup>rd</sup> flight)  
690 could be due to the imposed diurnal cycle on emissions (maxima at 18Z) in this version. The 3BEM  
691 version simulated the plume formation and downwind transport of smoke towards the Northeast  
692 during phase 1 but the decline in emissions in phase 2 resulted in a non-discernible plume with  
693 very low AOD enhancements. In comparison, the FRP version simulated a far more intense plume  
694 with AOD enhancements  $\geq 1$  near the fire and in the east/southwest direction. The plume  
695 coincided well with the sampling trajectory of the DC-8 indicating that the model simulated the  
696 spatial extent of the plume reasonably well. The estimated emissions for Williams Flats were lower  
697 for August 6<sup>th</sup> as compared to the other flight days, which resulted in the relatively lower AOD  
698 enhancements than those on August 3<sup>rd</sup>.

699

700

701



702

703 **Figure 8: AOD estimates for HSRL, GOES-16/17 and WRF-Chem (3BEM and FRP**  
 704 **versions) for the August 3 (d), August 6 (e) and August 7 (f) DC-8 science flights. The domain**  
 705 **over which the AODs are being compared are also shown (a-c). Each box plot represents the**  
 706 **minimum value, lower quartile, median, upper quartile and maximum value. The mean is**  
 707 **represented as the asterisk (\*) symbol in the bar and the outliers are represented by the star**  
 708 **symbols.**

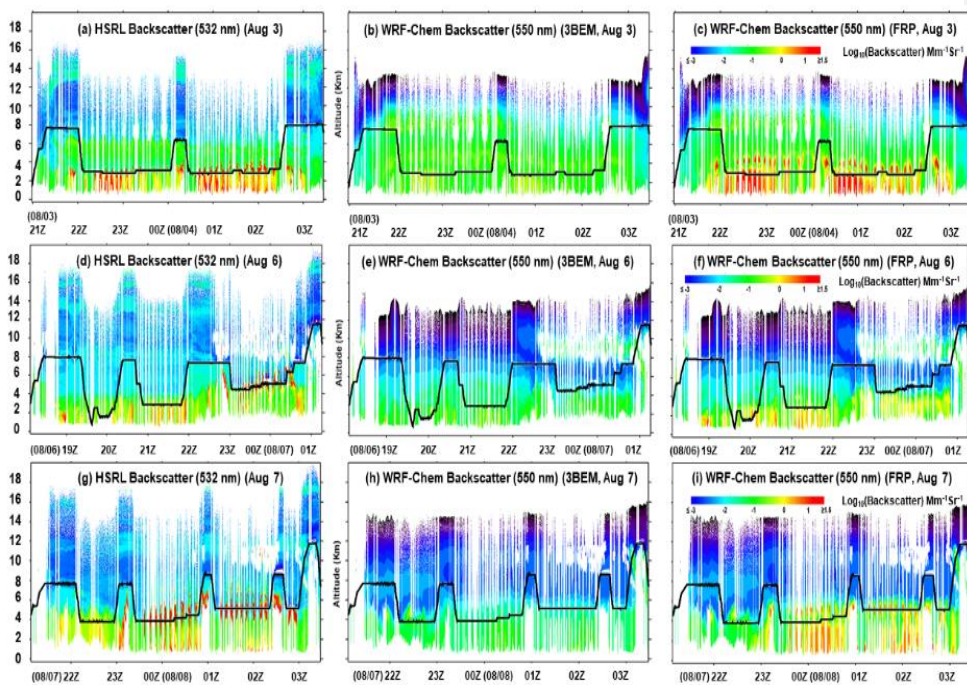
709 Figure 8 shows comparisons of AOD available from the GOES-16/17 ABI AOD product with the  
 710 simulated WRF-Chem AOD (3BEM and FRP versions) for all the DC-8 science flights. AOD  
 711 computed from the HSRL backscatter is also included. The HSRL AOD was computed by  
 712 multiplying the HSRL backscatter with the lidar ratio for BC/OC to estimate the extinction  
 713 coefficient and subsequently integrating the extinction coefficient. We only carry out these  
 714 comparisons for the Williams Flats fire in the spatial domains shown in Figure 8 (a-c). The  
 715 domains were chosen to include the fire as well as the region impacted by the fire plume and  
 716 sampled by the DC-8 during the respective science flights. We only consider the time periods  
 717 relevant to the DC-8 sampling of the Williams Flats fire (August 3: 22Z – 2:30Z, August 6: 19:30Z

718 – 22Z, August 7; 23Z – 2:30Z). In general, the GOES-16 AOD product had a low bias as compared  
719 to the GOES-17 AOD product both in the median (GOES-16: 0.26 – 0.29, GOES-17: 0.33 – 0.45)  
720 and extreme values, which could be due to the differences in availability of data from the two  
721 satellites during the time period considered. The HSRL AOD (median: 0.32-2) was the highest  
722 amongst all the data sources (except August 6<sup>th</sup>) and exhibited the most variability as well,  
723 reflecting the fine temporal and spatial resolution of the HSRL measurements. The significant  
724 underestimation of aerosol concentrations in the 3BEM version is evident here as well with the  
725 simulated median AOD values (0.07 – 0.24) and the extreme values being lower than that from  
726 the other data sources. This further indicates the inability of this version to capture the AOD  
727 enhancements observed near the fire and in the associated plume. The underestimation as  
728 compared to the FRP version (median: 0.24 – 0.78) has already been demonstrated and will not be  
729 discussed further. The AOD enhancements close to the Williams Flats fire were overestimated by  
730 the FRP version on August 3<sup>rd</sup> and August 7<sup>th</sup> (e.g., outlier values) as compared to GOES-16/17  
731 estimates, while on August 6<sup>th</sup> this version was biased low due to underestimation of emissions.  
732 The agreement on August 3<sup>rd</sup> and August 7<sup>th</sup> tended to be better farther away from the fire (e.g.,  
733 downwind plume) resulting in closer median AOD values for the FRP version (August 3<sup>rd</sup>: 0.78,  
734 August 7<sup>th</sup>: 0.43) as compared to GOES-16/17 (GOES-16: August 3<sup>rd</sup>: 0.26, August 7<sup>th</sup>: 0.29;  
735 GOES-17: August 3<sup>rd</sup>: 0.33, August 7<sup>th</sup>: 0.40). On the other hand, comparisons with HSRL<sub>AOD</sub>  
736 present an opposite picture with significant underestimation by the FRP version on August 6<sup>th</sup> and  
737 August 7<sup>th</sup> both near and far away from the fire.  
738 Potential caveats in these comparisons include the availability of GOES-16/17 data during the  
739 entire time period considered. There could be cases where data during the highest AOD periods is  
740 not available due to factors such as cloud cover. In addition, the procedure of computation of

741 aerosol optical properties in WRF-Chem could impact the computed AOD values (discussed later  
 742 in Section 4.6). Furthermore, the HSRL AOD is derived from the backscatter using literature lidar  
 743 ratio values rather than direct integration of the extinction profile. Overall, the general conclusions  
 744 that can be drawn from these comparisons are that the FRP version demonstrates the capability of  
 745 simulating the high AOD values which accompany major wildfire events. However, it also has the  
 746 tendency to overestimate the AOD when compared with the GOES-16/17 ABI AOD product.

747 **4.5.2. Aerosol Backscatter**

748



749

750 **Figure 9: FIREX-AQ DC-8 flight curtains for the DC-8 science flights for August 3 (a-c),**  
 751 **August 6 (d-f) and August 7 (g-i)**

752 [Figure 9](#) shows the curtains for HSRL aerosol backscatter coefficient (referred to as backscatter  
753 [hereon](#)) measurements ((a), (d), (g)) and the simulated WRF-Chem backscatter (3BEM ((b), (e),  
754 (h)) and FRP ((c), (f), (i)) versions) for the August 3<sup>rd</sup> – 7<sup>th</sup> DC-8 science flights. The DC-8 flight  
755 [track is also shown](#). For the August 3<sup>rd</sup> flight, the HSRL measurements ([Figure 9 \(a\)](#)) show the  
756 [plume from the Lick/Mica Creek fire](#) (~ between 21:00Z and 21:30Z) reaching an altitude of ~ 3  
757 km. These enhancements were underestimated by both the 3BEM ([Figure 9 \(b\)](#)) and FRP ([Figure](#)  
758 [9 \(c\)](#)) versions possibly due to an underestimation in emissions for this fire. The subsequent time  
759 periods in the HSRL observations represent the DC-8 sampling phases of Williams Flats. Between  
760 21:30Z and 22:00Z, the aircraft travelled across Williams Flats to begin phase 1 of sampling. The  
761 phase 1 sampling period began just after 22Z and continued downwind of the fire till 00Z followed  
762 by a return transit to the fire (between 00Z and 1Z) and phase 2. The HSRL measurements show  
763 an alternating sequence of high and low backscatter enhancements during phases 1 and 2, which  
764 represents the aircraft traversing laterally in and out of the plume. The 3BEM version simulated  
765 localized backscatter enhancements near the fire during the early stages of phase 1 (22Z – 23Z).  
766 These enhancements were lower than the HSRL observations and declined significantly as the  
767 aircraft moved downwind (23Z – 00Z) consistent with the observations. The enhancements in the  
768 downwind plume were underestimated. In phase 2, the 3BEM version simulated backscatter  
769 enhancements lower than that in phase 1 near the fire (00Z – 01Z) which continued to decline as  
770 the aircraft moved downwind. The lower enhancements in phase 2 as compared to phase 1 are  
771 consistent with the declining phase of the emissions diurnal cycle in the 3BEM version. Thus, the  
772 3BEM version showed several discrepancies with the HSRL measurements which included  
773 underestimation of backscatter near and downwind of the fire in both phases 1 and 2. The FRP  
774 version showed better overall agreement with the HSRL measurements simulating comparable

775 backscatter enhancements to the HSRL measurements during most parts of phases 1 and 2. The  
776 FRP version was also able to better capture the observed variation in the aerosol backscatter as the  
777 aircraft traversed in and out of the plume although the coarse spatial resolution of the model (8 km  
778 x 8 km) acts as a limitation in exactly simulating the observed variation from the center to the edge  
779 of the plume. In phases 1 and 2, the model simulated continuously high aerosol backscatter near  
780 the fire which was also observed by HSRL. It was also able to reproduce the variations in observed  
781 aerosol backscatter due to the closely spaced legs of the DC-8 flight near the fire and widely spaced  
782 legs of the DC-8 flight downwind of the fire in phase 1. For example, the alternate sequence of  
783 high/low aerosol backscatter is wider for the widely spaced legs of the flight (downwind of the  
784 fire) as compared to the closely spaced legs near the fire. The model was also able to reproduce  
785 the variation in backscatter observed downwind of the fire very well especially in phase 1. Thus,  
786 the model simulated a plume with high aerosol loadings near and extending a significant distance  
787 from the fire which was more consistent with the observed plume as is evident in the better  
788 agreement with the HSRL measurements. The FRP version appears to overestimate the plume  
789 height for several parts of the flight (e.g., either side of 22Z, at 03Z, phase 1 and transit phase  
790 before phase 2) but showed better agreement with the HSRL measurements in the latter part of  
791 phase 2 (after 01Z) when the fire had intensified.

792 Figure 9 (d-f) represents the August 6<sup>th</sup> DC-8 sampling of the Williams Flats fire during phase 1  
793 (between ~ 19:30Z and 20Z) and phase 2 (21Z to 22Z) and the Horsefly fire from 23Z to just  
794 before 00:30 Z. The backscatter enhancements during phase 1 (low level smoke sampling) were  
795 underestimated by the WRF-Chem 3BEM version while the FRP version tended to overestimate.  
796 The HSRL measurements (Figure 9 (d)) were not available near 20Z (below the DC-8) due to  
797 attenuation which precludes any further comparisons. During 20Z-21Z, the high backscatter in the

798 HSRL measurements correspond to Williams Flats as the DC-8 flew over the fire to begin phase  
799 2 of sampling. These enhancements were largely absent in the 3BEM version (Figure 9 (e)) but  
800 were reproduced well in the FRP version (Figure 9 (f)). During phase 2 of sampling (21Z-22Z),  
801 the 3BEM experiment only simulated sporadic backscatter enhancements which were biased low  
802 as compared to the HSRL measurements. The measurements showed consistently high backscatter  
803 as the DC-8 traversed along the plume with the alternating bands of high/low backscatter again  
804 reflecting the periods the aircraft was within the plume or entering/leaving it. The FRP version did  
805 a better job than the 3BEM version, simulating comparable backscatter enhancements to the HSRL  
806 measurements and represented the variation along the flight track well. The HSRL backscatter  
807 enhancements between 22Z-23Z were due to the Snow Creek and Horsefly fires and were better  
808 represented by the FRP version. For the Horsefly fire, the DC-8 travelled downwind in the plume  
809 starting at ~23Z and continuing sometime after 00Z, which was followed by an upwind pass. The  
810 3BEM version was biased low for this entire period consistent with the low emissions. The FRP  
811 version did simulate higher backscatter enhancements than the 3BEM version throughout this  
812 period, but it was unable to reproduce the peak enhancements in the HSRL measurements. In  
813 addition, WRF-Chem (3BEM and FRP) underestimated the plume height for Horsefly ( $\leq 4$  km)  
814 as compared to the HSRL observations ( $\sim 4 - 6$  km). Consequently, the variation of the backscatter  
815 enhancements along the flight track does not agree with the HSRL observations.

816 Figure 9 (g-i) shows the HSRL backscatter measurements and WRF-Chem backscatter (3BEM  
817 and FRP runs) for the August 7<sup>th</sup> flight. The HSRL measurements (Figure 9 (g)) show the aerosol  
818 layer height due to the aged Williams Flats plume extending close to 6 km which was simulated  
819 very well by both the 3BEM (Figure 9 (h)) and FRP runs (Figure 9 (i)) although both versions  
820 were biased low. The HSRL measurements showed very high aerosol backscatter during the period

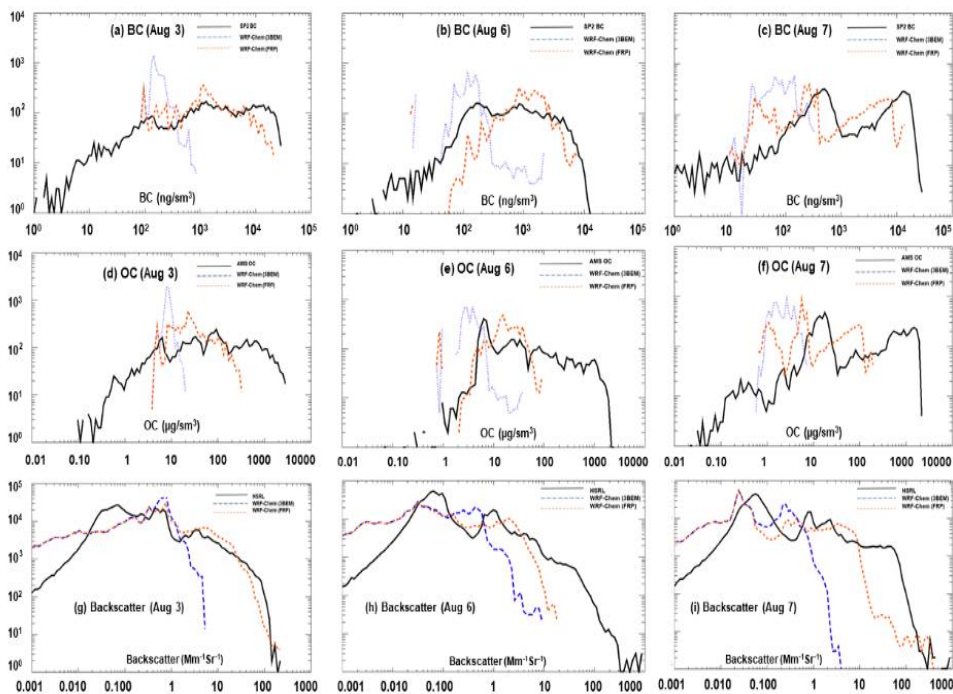


821 of fresh smoke sampling till ~ 7 km. This was reproduced well by the WRF-Chem FRP version,  
822 however the altitude was underestimated (~ 5.5- 6 km) and for the 3BEM run, the backscatter  
823 enhancements were very low. During phase 2 of the sampling as the DC-8 moved along the plume,  
824 the HSRL measurements showed high aerosol backscatter values throughout with plume heights  
825 extending till ~ 6 km. The 3BEM version failed to capture the observed enhancements and was  
826 biased low throughout the remainder of the flight mainly due to the low emissions. The FRP  
827 version consistently simulated significantly higher backscatter as compared to the 3BEM run and  
828 simulated the plume height between 5-6 km. The observed plume heights in phase 2 of the flight  
829 ranged from ~ 5 – 6.5 km and the backscatter levels were high as shown in the HSRL observations  
830 (01 – 02Z). The FRP version simulated enhancements comparable to the HSRL observations but  
831 was still biased low. The vertical extents were ~ 5-5.5 km which were in reasonable agreement  
832 with HSRL measurements. The backscatter observed during the last pass over the fire at 8 km  
833 altitude was also well simulated by the FRP version with a plume height of ~ 5.8 km matching  
834 well with that observed in the HSRL data (~ 6 km). During phase 4, the FRP version showed  
835 significantly better agreements with the HSRL observations with higher enhancements than the  
836 3BEM run and a predicted plume height of ~ 5 km agreeing very well with the HSRL observations  
837 (~ 5 km).

838 ~~**4.3. Statistical Comparison of WRF-Chem and FIREX-AQ**~~  
839 ~~**Measurements (BC and OC)**~~

840 **4.6. Statistical Comparison of WRF-Chem and FIREX-AQ**  
841 **Measurements**

842  
843 **4.6.1. Distributions of Aerosol Concentrations, optical properties, and plume heights**  
844



845 **Figure 10: Frequency distributions for BC (a-c), OC (d-f), backscatter coefficient (g-i) for**  
 846 **the August 3, August 6 and August 7 DC-8 science flights. Note: BC and OC only represent**  
 847 **in-plume cases.**

849

850 Figure 10 (a-i) shows the comparison of frequency distributions of the FIREX-AQ measurements  
 851 vs WRF-Chem (3BEM and FRP runs) for BC and OC, and the backscatter for the August 3<sup>rd</sup>-7<sup>th</sup>  
 852 DC-8 science flights. The BC and OC distributions only account for the cases when the aircraft  
 853 was in a smoke plume. The backscatter distributions are based on all observations during the flight  
 854 period. For BC and OC, during the August 3<sup>rd</sup> flight (Figure 10 (a), (b)), the in-situ measurements  
 855 spanned a wide range (BC: 1 to > 10<sup>4</sup> ng/sm<sup>3</sup> and OC: ~0.1 to ~3000 µg/sm<sup>3</sup>) which reflects the  
 856 contrasting aerosol concentrations in the environments in which the aircraft sampling occurred.  
 857 For example, sampling included the center/edges of the Williams Flats plume both near and a

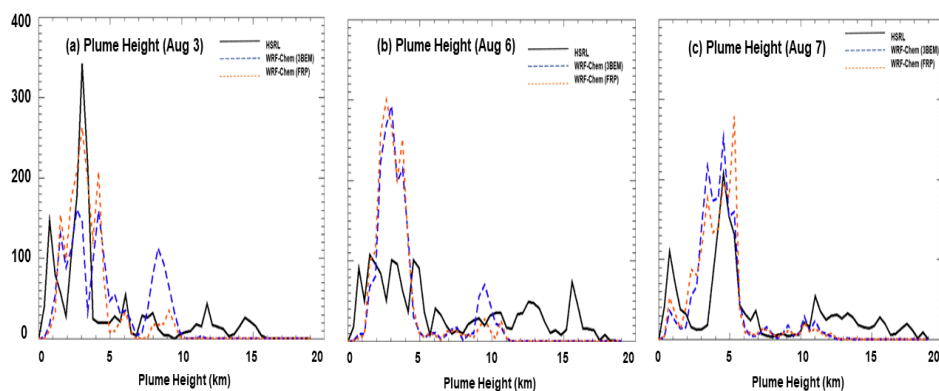
858 significant distance downwind from the fire as well as remnants of any pollution at high altitudes.  
859 Aerosol concentrations in both cases could be very different considering that the flight sampled  
860 fresh Williams Flats smoke while the pollution remnants at high altitudes would have undergone  
861 significant dilution and thus would have much lower aerosol concentrations. WRF-Chem (3BEM  
862 and FRP versions) showed less variability in the simulated BC and OC concentrations than the  
863 measurements which could be due to the coarse spatial resolution of the model and simplified  
864 chemical mechanism in the GOCART scheme. The 3BEM version captured very little of the  
865 observed variability in the BC and OC measurements distributions. It simulated BC concentrations  
866 most frequently between  $\sim 80\text{-}250\text{ ng/sm}^3$  and OC concentrations between  $\sim 4\text{-}10\text{ }\mu\text{g/sm}^3$  with a  
867 small fraction of higher values (BC:  $250\text{-}900\text{ ng/m}^3$ , OC:  $10\text{-}11\text{ }\mu\text{g/sm}^3$ ). The FRP version had an  
868 identical distribution for the lower end of concentrations (BC:  $80\text{-}100\text{ ng/sm}^3$ , OC:  $4\text{-}6\text{ }\mu\text{g/sm}^3$ )  
869 which is representative of the remote atmosphere and high altitudes where the impacts of changes  
870 in emissions and the plume rise are negligible. The FRP version was able to reproduce the observed  
871 distribution to a much better extent, especially for the high BC and OC concentrations (BC  $> 105$   
872  $\text{ng/sm}^3$ , OC  $> 80\text{ }\mu\text{g/sm}^3$ ) relevant for large wildfire events, reflecting the impacts of higher  
873 emissions. The high biases in both versions of the model for the frequency of lower end  
874 concentrations (BC  $< 80\text{ ng/sm}^3$ , OC  $< 3\text{ }\mu\text{g/sm}^3$ ) could correspond to the cases when the DC-8  
875 was at the plume-edge or when environments with low aerosol concentrations were being sampled  
876 (e.g., the long-range transport plume). The model with its coarse spatial resolution ( $8\text{km} \times 8\text{km}$ )  
877 could not accurately simulate the variability observed while transiting from the center of the plume  
878 to the edges. The observed distributions for BC and OC for the August 6<sup>th</sup> flight ([Figure 10 \(d\)](#),  
879 [\(e\)](#)) represented a similar range of in-plume concentrations as the August 3<sup>rd</sup> flight, however, the  
880 lower end of concentrations were higher for BC and OC, possibly due to this flight focusing only

881 on fresh smoke sampling unlike the August 3<sup>rd</sup> flight which also sampled aged smoke (long-range  
882 transport plume). The significant variance of the BC and OC distribution also reflects the various  
883 sampling conditions such as the aircraft traversing through the plume encountering high  
884 concentrations at the center and lower concentrations towards the edges, the different altitudes of  
885 sampling (phase 1 at lower altitude and phase 2 at higher altitude for Williams Flats) and traversing  
886 downwind from the Williams Flats and Horsefly fires. Similar to the August 3<sup>rd</sup> flight, the WRF-  
887 Chem BC and OC distributions could not capture all the variability in the observations and were  
888 also biased high primarily due to the coarse model resolution, which precluded accurate simulation  
889 of the observed variability from the plume center to the edges. The 3BEM version distribution was  
890 able to better capture the variability in the BC and OC distributions than for the August 3<sup>rd</sup> flight,  
891 which was mainly due to the better simulation of BC and OC concentrations in the low-altitude  
892 Williams Flats smoke. However, it still had a low bias compared to BC and OC measurements.  
893 The FRP version showed good agreement with the BC distribution although it was biased low for  
894 OC. The low bias could primarily be attributed to the underestimation during the Horsefly  
895 sampling phase and the simplified chemistry in the GOCART mechanism (no SOA). Nevertheless,  
896 the distributions for the FRP version showed both an increase in variability and a shift towards  
897 higher simulated BC and OC concentrations. This resulted in better simulation of the variability in  
898 the BC and OC measurements distribution as compared to the 3BEM version and better agreement  
899 with the observed BC and OC distributions at concentration levels relevant for fire plumes. For  
900 the August 7<sup>th</sup> flight, the observed distributions for BC and OC ([Figure 10 \(g\), \(h\)](#)) were similar to  
901 the previous flights, exhibiting high variability due to the sampling of a wide range of aerosol  
902 loading environments. For example, the Williams Flats aged plume was characterized by  
903 significantly lower aerosol concentrations as compared to the fresh plume sampled later. In

904 addition, similar to the previous flights, the concentrations at the edge and center of the plume  
905 would also contribute to the variability observed in the BC and OC observations distributions.  
906 WRF-Chem (FRP version) was able to reproduce a significant fraction of this variability for BC  
907 and OC particularly for the high concentrations, as shown in corresponding distributions.

908 The backscatter distributions were similar to the BC and OC distributions except that the model  
909 was closer to the measurements (e.g., August 3<sup>rd</sup> and August 7<sup>th</sup> flights [\(Figure 10 \(g\), \(i\)\)](#) even  
910 though it was underestimating BC and OC. A potential reason for this discrepancy could be that  
911 we use lidar ratios from previous work in deriving the backscatter from the WRF-Chem aerosol  
912 extinction coefficient. In addition, meteorological parameters (e.g., relative humidity) and multiple  
913 aerosol species properties are used in computation of aerosol optical properties which could result  
914 in biases in the estimation. For the August 3<sup>rd</sup> flight, the backscatter distributions were identical  
915 for the 3BEM and FRP versions for low values ( $< 0.7 \text{ Mm}^{-1}\text{Sr}^{-1}$ ). These values could represent the  
916 high altitude phases of the flight during transition from Boise to Williams Flats where the effects  
917 due to fires would not be a factor. Similar to the BC and OC distributions, the FRP version captured  
918 the observed backscatter distribution well especially for the higher values which were due to  
919 Williams Flats. The backscatter distribution derived from the HSRL measurements for the August  
920 6<sup>th</sup> flight [\(Figure 10 \(h\)\)](#) showed similar characteristics with lower values ( $< 0.01$ ) primarily  
921 representing very high altitudes with no influence of fire emissions. This region was identically  
922 simulated by WRF-Chem (3BEM and FRP) since the primary differences between the two  
923 versions (fire emissions and plume-rise) had little/no effects at these altitudes. The backscatter  
924 distribution also exhibited considerable variability (values spanned six orders of magnitude) which  
925 was consistent with the high variability observed in the BC and OC distributions. The backscatter  
926 distribution for the FRP version also showed a shift towards simulating higher enhancements than

927 the 3BEM version and showing better agreement with the HSRL distribution at backscatter levels  
928 relevant to major fire events. The backscatter distribution of the FRP version also showed better  
929 agreement with the HSRL backscatter distribution. These major changes, which were also found  
930 in earlier flights, includes a significant shift in the BC and OC backscatter distributions towards  
931 higher values and better agreement with observations.



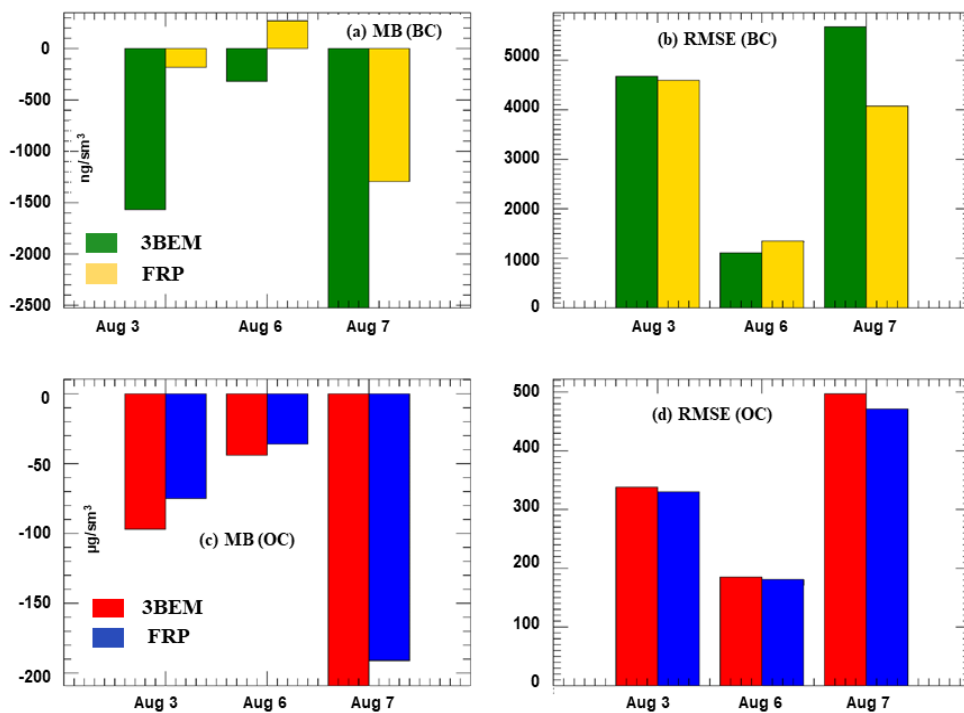
932  
933 **Figure 11: Frequency distributions for estimated plume heights for the August 3 (a), August**  
934 **6 (b) and August 7 (c) DC-8 science flights.**

935  
936 Figure 11 (a-c) shows the estimated plume height distributions from the HSRL measurements  
937 along with the simulated plume heights from WRF-Chem (3BEM and FRP versions). For the  
938 August 3<sup>rd</sup> flight (Figure 11 (a)), the best estimated plume heights based on HSRL observations  
939 were ~ 3 km (represented by the highest peak in Figure 11 (a)) during the flight. In contrast, both  
940 3BEM and FRP versions showed additional peaks in their distribution functions on either side of  
941 the observed peak. Therefore, the predicted plume heights varied between 2.7 – 4.1 km for the  
942 3BEM version and 3 – 4.1 km for the FRP version. The FRP version did produce a better agreement  
943 with the observed plume heights based on the highest peak in the distribution function but also  
944 overestimated the heights for some parts of the flight. Moreover, the low elevation smoke

945 (represented by the peak < 1 km in HSRL) was either not captured or overestimated (peak ~ 1.5  
946 km) by both WRF-Chem versions. The plume heights distribution ([August 6<sup>th</sup> flight, Figure 11](#)  
947 [\(b\)](#)) based on HSRL measurements showed several peaks which could be attributed to the multiple  
948 altitudes at which smoke was sampled during this flight. Based on the observed peaks, the heights  
949 could have ranged from 0.75 km to 6 km. The heights between 3 – 6 km are associated with the  
950 high altitude Williams Flats plume and the Horsefly fire plume while the < 3 km altitude are from  
951 the lower altitude Williams Flats smoke. Neither WRF-Chem versions could capture this  
952 variability in the observed plume heights distribution and simulated smoke heights of ~ 3km (peak  
953 1) and ~ 3.8 km (peak 2) for the 3BEM version (~ 2.7 and ~ 3.8 km for the FRP version). Thus,  
954 WRF-Chem underestimated the plume heights for this flight, which as discussed earlier in this  
955 section, could be a possible reason for the sharp decline in the simulated BC and OC concentrations  
956 as the DC-8 proceeded downwind of the Horsefly fire. For the August 7<sup>th</sup> flight, the estimated  
957 plume heights from HSRL showed one prominent peak near 5 km which would correspond to the  
958 Williams Flats smoke (aged and fresh). For the WRF-Chem 3BEM version, the simulated plume  
959 height varied between 3.5~ 5 km (based on the two peaks in the distribution), while the FRP  
960 version varied from 3.5 – 5.5 km. Thus, both versions showed significant variability in the plume  
961 heights which could be due to different simulated injection heights in the model.

#### 962 [4.6.2. Statistical Metrics for BC and OC comparisons](#)

963



964 **Figure 12: Statistical metrics of comparisons for BC and OC for the August 3, August 6 and**  
 965 **August 7 DC-8 science flights. The average bias (MAB) and the root mean squared error**  
 966 **(RMSE) for BC (a, b) and OC (c, d) are shown.**  
 967

968  
 969 Figure 12 shows statistical metrics of comparisons between the WRF-Chem simulated BC and OC  
 970 and the SP2 and AMS observations for the respective species for all FIREX-AQ DC-8 flights  
 971 considered in this work. The statistics reported are:

- 972 1.) *Average Mean bias (MAB)*  $= \left(\frac{1}{N}\right) \sum_{i=1}^N (X_{WRF-Chem_i} - X_{Obs_i})$   
 973 2.) *Root Mean Squared Error (RMSE)*  $= \sqrt{\left(\frac{1}{N}\right) \sum_{i=1}^N (X_{WRF-Chem_i} - X_{Obs_i})^2}$



974 The 3BEM version had a low bias for both BC and OC, which was reduced significantly in the  
975 WRF-Chem FRP version. The MB and RMSE were reduced for the August 3<sup>rd</sup> flight (MB: 88%  
976 (BC) and 23% (OC), RMSE: 2% (BC) and 2.4% (OC)) and August 7<sup>th</sup> flight (MB: 49% (BC) and  
977 9% (OC), RMSE: 28% (BC) and 5.2% (OC)) which was primarily due to the better agreement of  
978 the simulated BC/OC concentrations in the fresh smoke sampling phases of both flights. However,  
979 the model still underestimates BC/OC as indicated by the negative MB values. The only exception  
980 was the August 6<sup>th</sup> flight, for which the performance of the FRP version degraded (only for BC)  
981 as compared to the 3BEM version. The MB and RMSE for BC increased primarily due to the  
982 significant overestimation of BC during the low level smoke sampling period (Figure 5 (d) 19-  
983 20Z). The overestimation was larger for BC, therefore MB and RMSE were worse than those for  
984 OC. The significantly better model performance with the FRP version was partly offset by the  
985 inability of the model to simulate the aged part of the Williams Flats fire. For BC, the 3BEM  
986 version had a low bias which was reduced significantly in the WRF-Chem FRP version. However,  
987 the model was still underestimating BC as indicated by the negative MAB values. For the August  
988 6<sup>th</sup> flight, the WRF-Chem FRP version had a positive MAB which could be due to the significant  
989 overestimation of BC during the low level smoke sampling period (Figure 10 (b) 19-20Z). This  
990 also contributes to the higher RMSE for the FRP version. For OC, the model performance  
991 improved across all flights with a significant reduction in the MAB and lower RMSE values than  
992 the 3BEM version. The improvements in model simulated aerosols were offset by the inability of  
993 the model to simulate the aged part of the Williams Flats fire.

## 994 **5. Conclusions**

995 This study employs the Weather Research and Forecasting with Chemistry (WRF-Chem) model  
996 (retrospective simulations) with GOES-16 FRP based methodologies to estimate wildfire

997 emissions, simulate wildfire plumerise and diurnal cycles to interpret in-situ and remote-sensing  
998 measurements collected aboard the NASA DC-8 aircraft during the 2019 NASA-NOAA FIREX-  
999 AQ field campaign and perform model evaluations. The primary focus is on the August 3<sup>rd</sup> -7<sup>th</sup>,  
1000 2019, science flights that sampled the Williams Flats fire in Washington. Main conclusions from  
1001 this evaluation are as follows:

1002 1.) The FIREX-AQ observations were characterized by a variety of aerosol loading environments  
1003 which resulted in a large range of BC/OC and aerosol backscatter values during the August 3<sup>rd</sup> -  
1004 7<sup>th</sup> science flights. These environments included fresh and aged smoke from Williams Flats and  
1005 high-altitude remnants of a plume that could have undergone long-range transport. The altitudes  
1006 of sampled smoke ranged from low-altitude (August 6<sup>th</sup>) to a pyro-Cb~~Pyro-Cb~~ (August 8).

1007 2.) The GOES-16 FRP based emissions employing the HRRR-Smoke methodology are  
1008 substantially higher than the standard emissions inventory (Freitas et al., 2011) in WRF-Chem  
1009 v3.5.1.

1010 3.) Wildfire emissions in the standard WRF-Chem (3BEM version) resulted in significant  
1011 underestimation of carbonaceous aerosol (BC and OC) concentrations observed during the  
1012 Williams Flats sampling flights in FIREX-AQ. The implementation of FRP based emissions  
1013 resulted in better agreement of model simulated BC and OC concentrations when compared to in-  
1014 situ BC and OC measurements, thereby showing potential to improve the capability of WRF-Chem  
1015 in simulating the high BC and OC enhancements observed during large wildfire events like the  
1016 Williams Flats fire.

1017 4.) The simulated plume heights in the WRF-Chem FRP version did not show as large of changes  
1018 as the emissions. The HRRR-Smoke FRP-based plume-rise methodology produced similar plume

1019 height distributions to the standard plumerise approach included in WRF-Chem v3.5.1 (Freitas et  
1020 al., 2007;2010). ~~Thus, the better performance of the WRF-Chem FRP version was mainly driven~~  
1021 ~~by the higher emissions in the FRP-based version. However, subtle differences were found during~~  
1022 ~~the flights considered. The aged Williams Flats plume in Montana was not distinctively simulated~~  
1023 ~~(August 7 flight) while the plume heights were lower for the Horsefly fire on August 6.~~

1024 5.) The diurnal cycle imposed on wildfire emissions in WRF-Chem was also an important factor.  
1025 For multiple flights, the standard WRF-Chem v3.5.1 with a diurnal cycle peaking at 18UTC  
1026 (Freitas et al., 2011) simulated declining emissions, AOD, and BC and OC concentrations during  
1027 the latter stages of the science flights-while observations often showed increases during these  
1028 periods. This shortcoming was not found in the FRP-version which employed new FRP based  
1029 diurnal cycle functions accounting for the variation with longitude.

1030 6.) WRF-Chem with the simplified GOCART mechanism could not adequately reproduce the  
1031 aerosol concentrations in the aged smoke (1 day ~~of or~~ more of aging). This was observed for all  
1032 science flights that sampled aged smoke from Williams Flats. ~~In addition to the primary factors~~  
1033 ~~such as emissions, plume-height and wildfire diurnal cycle estimation, second-order issues like~~  
1034 ~~biases in the aerosol dynamics (simulation of aerosol loss processes/transport) or chemistry (e.g.,~~  
1035 ~~no SOA in GOCART) could play a role here. It would be worthwhile to evaluate these flights in~~  
1036 ~~the future with a more comprehensive chemistry mechanism (including SOA) to better understand~~  
1037 ~~the underlying causes. The potential reasons for this could be biases in the aerosol dynamics~~  
1038 ~~(simulation of aerosol loss processes/transport) or chemistry (e.g., no SOA in GOCART).~~

1039

1040 Overall, the implementation of HRRR-Smoke FRP based methodologies in WRF-Chem resulted  
1041 in significantly better chemical forecasts ~~improvements in the WRF-Chem forecasts~~ for large  
1042 wildfire events like the Williams Flats fire. ~~These~~ improvements in chemical forecasts could  
1043 translate into better estimates of impacts of large wildfire events on human health, which is a cause  
1044 of concern given the current/future trends in wildfire activity in the US. ~~The~~ se comparisons  
1045 between the 3BEM and HRRR-Smoke FRP based emissions methodologies shown in this study  
1046 also demonstrate that the HRRR-Smoke FRP based emissions show the potential to improve the  
1047 forecast capability during major fire events and would be useful to be incorporated in  
1048 computational models providing air quality forecasts.

1049 **Author Contributions:** RBP conceptualized, supervised the study and developed the FRP based  
1050 diurnal cycle functions. AK did the PREP-Chem (emissions), WRF-Chem (plumerise)  
1051 development and carried out the WRF-Chem simulations. RBP and AK analyzed the FIREX-AQ  
1052 and WRF-Chem data. AK wrote the manuscript draft with contributions from the co-authors. RA,  
1053 GP, SF and GG developed the original HRRR-Smoke methodologies. CS provided the GOES-16  
1054 data. AL helped with setting up the WRF-Chem simulations. JPS, AEP, JMK provided the SP2-  
1055 BC and fire flags data. JH provided the HSRL data. JLJ, PCJ and HG provided the AMS-OC data.

1056 **Code/Data Availability:** FIREX-AQ measurements are available at:  
1057 [https://doi.org/10.5067/ASDC/FIREXAO\\_Aerosol\\_AircraftInSitu\\_DC8\\_Data\\_1](https://doi.org/10.5067/ASDC/FIREXAO_Aerosol_AircraftInSitu_DC8_Data_1)). The HSRL  
1058 data are available at:  
1059 [https://doi.org/10.5067/ASDC/FIREXAO\\_HSRL\\_AircraftRemoteSensing\\_DC8\\_Data\\_1](https://doi.org/10.5067/ASDC/FIREXAO_HSRL_AircraftRemoteSensing_DC8_Data_1)).

1060 **Competing Interests:** The authors declare that they have no conflict of interest.

1061 **Acknowledgements:** We acknowledge funding support from the NOAA CPO AC4 grant. We  
1062 would like to thank the FIREX-AQ leadership, the FIREX-AQ Science Team and the flight crews  
1063 for their contributions towards the success of the campaign. [We would also like to thank Z.H.](#)  
1064 [Zhang for providing the GOES-16/17 aerosol optical depth data.](#)

## 1065 **References**

1066 Ahmadov, R., Grell, G., James, E., Csiszar, I., Tsidulko, M., Pierce, B., McKeen, S., Benjamin, S., Alexander,  
1067 C., and Pereira, G.: Using VIIRS fire radiative power data to simulate biomass burning emissions, plume  
1068 rise and smoke transport in a real-time air quality modeling system, 2017 IEEE International Geoscience  
1069 and Remote Sensing Symposium (IGARSS), 2017, 2806-2808.

1070 Aiken, A. C., Decarlo, P. F., Kroll, J. H., Worsnop, D. R., Huffman, J. A., Docherty, K. S., Ulbrich, I. M.,  
1071 Mohr, C., Kimmel, J. R., and Sueper, D.: O/C and OM/OC ratios of primary, secondary, and ambient  
1072 organic aerosols with high-resolution time-of-flight aerosol mass spectrometry, *Environmental science &*  
1073 *technology*, 42, 4478-4485, 2008.

1074 Al-Saadi, J., Szykman, J., Pierce, R. B., Kittaka, C., Neil, D., Chu, D. A., Remer, L., Gumley, L., Prins, E., and  
1075 Weinstock, L.: Improving national air quality forecasts with satellite aerosol observations, *Bulletin of the*  
1076 *American Meteorological Society*, 86, 1249-1262, 2005.

1077 Al-Saadi, J. A., Soja, A. J., Pierce, R. B., Szykman, J. J., Wiedinmyer, C., Emmons, L. K., Kondragunta, S.,  
1078 Zhang, X., Kittaka, C., and Schaack, T.: Intercomparison of near-real-time biomass burning emissions  
1079 estimates constrained by satellite fire data, *Journal of Applied Remote Sensing*, 2, 021504, 2008.

1080 Andreae, M. O., and Merlet, P.: Emission of trace gases and aerosols from biomass burning, *Global*  
1081 *biogeochemical cycles*, 15, 955-966, 2001.

1082 Andreae, M. O.: Emission of trace gases and aerosols from biomass burning—an updated assessment,  
1083 *Atmospheric Chemistry and Physics*, 19, 8523-8546, 2019.

1084 Arakawa, A., and Lamb, V. R.: Computational design of the basic dynamical processes of the UCLA  
1085 general circulation model, *General circulation models of the atmosphere*, 17, 173-265, 1977.

1086 Bahreini, R., Ervens, B., Middlebrook, A., Warneke, C., De Gouw, J., DeCarlo, P., Jimenez, J., Brock, C.,  
1087 Neuman, J., and Ryerson, T.: Organic aerosol formation in urban and industrial plumes near Houston and  
1088 Dallas, Texas, *Journal of Geophysical Research: Atmospheres*, 114, 2009.

1089 Baylon, P. M., Jaffe, D. A., Pierce, R. B., and Gustin, M. S.: Interannual variability in baseline ozone and its  
1090 relationship to surface ozone in the western US, *Environmental science & technology*, 50, 2994-3001,  
1091 2016.

1092 Belward, A.: The IGBP-DIS global 1 km land cover data set (DISCover)-proposal and implementation  
1093 plans, IGBP-DIS Working Paper No. 13, T, Toulouse, France, 1996.

1094 Bond, W. J., Woodward, F. I., and Midgley, G. F.: The global distribution of ecosystems in a world  
1095 without fire, *New phytologist*, 165, 525-538, 2005.

1096 Burton, S., Ferrare, R., Hostetler, C., Hair, J., Rogers, R., Obland, M., Butler, C., Cook, A., Harper, D., and  
1097 Froyd, K.: Aerosol classification using airborne High Spectral Resolution Lidar measurements—  
1098 methodology and examples, *Atmospheric Measurement Techniques*, 5, 73-98, 2012.

1099 Canagaratna, M., Jimenez, J., Kroll, J., Chen, Q., Kessler, S., Massoli, P., Hildebrandt Ruiz, L., Fortner, E.,  
1100 Williams, L., and Wilson, K.: Elemental ratio measurements of organic compounds using aerosol mass  
1101 spectrometry: characterization, improved calibration, and implications, *Atmospheric Chemistry and*  
1102 *Physics*, 15, 253-272, 2015.

1103 Carter, T. S., Heald, C. L., Jimenez, J. L., Campuzano-Jost, P., Kondo, Y., Moteki, N., Schwarz, J. P.,  
1104 Wiedinmyer, C., Darmenov, A. S., and Silva, A. M. d.: How emissions uncertainty influences the  
1105 distribution and radiative impacts of smoke from fires in North America, *Atmospheric Chemistry and*  
1106 *Physics*, 20, 2073-2097, 2020.

1107 Chen, F., and Dudhia, J.: Coupling an advanced land surface–hydrology model with the Penn State–NCAR  
1108 MM5 modeling system. Part I: Model implementation and sensitivity, *Monthly weather review*, 129,  
1109 569-585, 2001.

1110 Chin, M., Rood, R. B., Lin, S. J., Müller, J. F., and Thompson, A. M.: Atmospheric sulfur cycle simulated in  
1111 the global model GOCART: Model description and global properties, *Journal of Geophysical Research:*  
1112 *Atmospheres*, 105, 24671-24687, 2000a.

1113 Chin, M., Savoie, D. L., Huebert, B. J., Bandy, A. R., Thornton, D. C., Bates, T. S., Quinn, P. K., Saltzman, E.  
1114 S., and De Bruyn, W. J.: Atmospheric sulfur cycle simulated in the global model GOCART: Comparison  
1115 with field observations and regional budgets, *Journal of Geophysical Research: Atmospheres*, 105,  
1116 24689-24712, 2000b.

1117 Chin, M., Ginoux, P., Kinne, S., Torres, O., Holben, B. N., Duncan, B. N., Martin, R. V., Logan, J. A.,  
1118 Higurashi, A., and Nakajima, T.: Tropospheric aerosol optical thickness from the GOCART model and  
1119 comparisons with satellite and Sun photometer measurements, *Journal of the atmospheric sciences*, 59,  
1120 461-483, 2002.

1121 Darmenov, A. S., and da Silva, A.: The Quick Fire Emissions Dataset (QFED): Documentation of versions  
1122 2.1, 2.2 and 2.4Rep. TM–2015–104606 NASA, in, 212, 2015.

1123 Deanes, L. N., Ahmadov, R., McKeen, S. A., Manross, K., Grell, G. A., and James, E.: Evaluation of High  
1124 Resolution Rapid Refresh-Smoke (HRRR-Smoke) model products for a case study using surface PM<sub>2.5</sub>  
1125 observations, AGU Fall Meeting Abstracts, 2016, A51D-0100.

1126 DeCarlo, P. F., Kimmel, J. R., Trimborn, A., Northway, M. J., Jayne, J. T., Aiken, A. C., Gonin, M., Fuhrer, K.,  
1127 Horvath, T., and Docherty, K. S.: Field-deployable, high-resolution, time-of-flight aerosol mass  
1128 spectrometer, *Analytical chemistry*, 78, 8281-8289, 2006.

1129 Dozier, J.: A method for satellite identification of surface temperature fields of subpixel resolution,  
1130 *Remote Sensing of environment*, 11, 221-229, 1981.

1131 Fairlie, T. D., Avery, M. A., Pierce, R. B., Al-Saadi, J., Dibb, J., and Sachse, G.: Impact of multiscale  
1132 dynamical processes and mixing on the chemical composition of the upper troposphere and lower  
1133 stratosphere during the Intercontinental Chemical Transport Experiment–North America, *Journal of*  
1134 *Geophysical Research: Atmospheres*, 112, 2007.

1135 Flannigan, M. D., Stocks, B. J., and Wotton, B. M.: Climate change and forest fires, *Science of the total*  
1136 *environment*, 262, 221-229, 2000.

1137 Freitas, S., Longo, K., Trentmann, J., and Latham, D.: Sensitivity of 1-D smoke plume rise models to the  
1138 inclusion of environmental wind drag, *Atmospheric Chemistry and Physics*, 10, 585-594, 2010.

1139 Freitas, S., Longo, K., Alonso, M. a., Pirre, M., Marecal, V., Grell, G., Stockler, R., Mello, R., and Sánchez  
1140 Gácita, M.: PREP-CHEM-SRC–1.0: a preprocessor of trace gas and aerosol emission fields for regional and  
1141 global atmospheric chemistry models, *Geoscientific Model Development*, 4, 419-433, 2011.

1142 Freitas, S. R., Longo, K. M., Chatfield, R., Latham, D., Silva Dias, M., Andreae, M., Prins, E., Santos, J.,  
1143 Gielow, R., and Carvalho Jr, J.: Including the sub-grid scale plume rise of vegetation fires in low  
1144 resolution atmospheric transport models, *Atmospheric Chemistry and Physics*, 7, 3385-3398, 2007.

1145 Gibbs, H. K.: Olson’s Major World Ecosystem Complexes Ranked by Carbon in Live Vegetation: An  
1146 Updated Database Using the

1147 GLC2000 Land Cover Product, NDP-017b, available at:  
1148 <http://cdiac.ornl.gov/epubs/ndp/ndp017/ndp017b.html>, Carbon Dioxide Information Center, Oak Ridge  
1149 National Laboratory, Oak Ridge, Tennessee, 2006.

1150 Gibbs, H. K., Brown, S., Niles, J. O., and Foley, J. A.: Monitoring and estimating tropical forest carbon  
1151 stocks: making REDD a reality, *Environmental research letters*, 2, 045023, 2007.

1152 Giglio, L., and Kendall, J. D.: Application of the Dozier retrieval to wildfire characterization: A sensitivity  
1153 analysis, *Remote Sensing of Environment*, 77, 34-49, 2001.

1154 Giglio, L., Schroeder, W., and Justice, C. O.: The collection 6 MODIS active fire detection algorithm and  
1155 fire products, *Remote Sensing of Environment*, 178, 31-41, 2016.

1156 Ginoux, P., Chin, M., Tegen, I., Prospero, J. M., Holben, B., Dubovik, O., and Lin, S. J.: Sources and  
1157 distributions of dust aerosols simulated with the GOCART model, *Journal of Geophysical Research:  
1158 Atmospheres*, 106, 20255-20273, 2001.

1159 Greenwald, T. J., Pierce, R. B., Schaack, T., Otkin, J., Rogal, M., Bah, K., Lenzen, A., Nelson, J., Li, J., and  
1160 Huang, H.-L.: Real-time simulation of the GOES-R ABI for user readiness and product evaluation, *Bulletin  
1161 of the American Meteorological Society*, 97, 245-261, 2016.

1162 Grell, G. A., Peckham, S. E., Schmitz, R., McKeen, S. A., Frost, G., Skamarock, W. C., and Eder, B.: Fully  
1163 coupled "online" chemistry within the WRF model, *Atmospheric Environment*, 39, 6957-6975, 2005.

1164 Grell, G. A., and Freitas, S. R.: A scale and aerosol aware stochastic convective parameterization for  
1165 weather and air quality modeling, *Atmospheric Chemistry and Physics*, 14, 5233-5250, 2014.

1166 Guo, H., Campuzano-Jost, P., Nault, B. A., Day, D. A., Schroder, J. C., Kim, D., Dibb, J. E., Dollner, M.,  
1167 Weinzierl, B., and Jimenez, J. L.: The importance of size ranges in aerosol instrument intercomparisons: a  
1168 case study for the Atmospheric Tomography Mission, *Atmospheric Measurement Techniques*, 14, 3631-  
1169 3655, 2021.

1170 Hair, J. W., Hostetler, C. A., Cook, A. L., Harper, D. B., Ferrare, R. A., Mack, T. L., Welch, W., Izquierdo, L.  
1171 R., and Hovis, F. E.: Airborne high spectral resolution lidar for profiling aerosol optical properties,  
1172 *Applied optics*, 47, 6734-6752, 2008.

1173 Halofsky, J. E., Peterson, D. L., and Harvey, B. J.: Changing wildfire, changing forests: the effects of  
1174 climate change on fire regimes and vegetation in the Pacific Northwest, USA, *Fire Ecology*, 16, 1-26,  
1175 2020.

1176 Hodzic, A., Campuzano-Jost, P., Bian, H., Chin, M., Colarco, P. R., Day, D. A., Froyd, K. D., Heinold, B., Jo,  
1177 D. S., and Katich, J. M.: Characterization of organic aerosol across the global remote troposphere: a  
1178 comparison of ATom measurements and global chemistry models, *Atmospheric Chemistry and Physics*,  
1179 20, 4607-4635, 2020.

1180 Holden, Z. A., Swanson, A., Luce, C. H., Jolly, W. M., Maneta, M., Oyler, J. W., Warren, D. A., Parsons, R.,  
1181 and Affleck, D.: Decreasing fire season precipitation increased recent western US forest wildfire activity,  
1182 *Proceedings of the National Academy of Sciences*, 115, E8349-E8357, 2018.

1183 Hong, S.-Y., Dudhia, J., and Chen, S.-H.: A revised approach to ice microphysical processes for the bulk  
1184 parameterization of clouds and precipitation, *Monthly weather review*, 132, 103-120, 2004.

1185 Hong, S.-Y., Noh, Y., and Dudhia, J.: A new vertical diffusion package with an explicit treatment of  
1186 entrainment processes, *Monthly weather review*, 134, 2318-2341, 2006.

1187 Hong, S.-Y., and Jang, J.: Impacts of shallow convection processes on a simulated boreal summer  
1188 climatology in a global atmospheric model, *Asia-Pacific Journal of Atmospheric Sciences*, 54, 361-370,  
1189 2018.

1190 Huang, M., Carmichael, G. R., Pierce, R. B., Jo, D. S., Park, R. J., Flemming, J., Emmons, L. K., Bowman, K.  
1191 W., Henze, D. K., and Davila, Y.: Impact of intercontinental pollution transport on North American ozone  
1192 air pollution: an HTAP phase 2 multi-model study, *Atmospheric chemistry and physics*, 17, 5721-5750,  
1193 2017.

1194 Iacono, M. J., Delamere, J. S., Mlawer, E. J., Shephard, M. W., Clough, S. A., and Collins, W. D.: Radiative  
1195 forcing by long-lived greenhouse gases: Calculations with the AER radiative transfer models, *Journal of  
1196 Geophysical Research: Atmospheres*, 113, 2008.

1197 Jaffe, D. A., O'Neill, S. M., Larkin, N. K., Holder, A. L., Peterson, D. L., Halofsky, J. E., and Rappold, A. G.:  
1198 Wildfire and prescribed burning impacts on air quality in the United States, *Journal of the Air & Waste*  
1199 *Management Association*, 70, 583-615, 2020.

1200 Janić, Z. I.: Nonsingular implementation of the Mellor-Yamada level 2.5 scheme in the NCEP Meso  
1201 model, 2002.

1202 Janjic, Z.: The surface layer parameterization in the NCEP Eta Model, *World Meteorological*  
1203 *Organization-Publications-WMO TD*, 4.16-14.17, 1996.

1204 Jiang, Y., Yang, X.-Q., Liu, X., Qian, Y., Zhang, K., Wang, M., Li, F., Wang, Y., and Lu, Z.: Impacts of wildfire  
1205 aerosols on global energy budget and climate: The role of climate feedbacks, *Journal of Climate*, 33,  
1206 3351-3366, 2020.

1207 Jimenez, J. L., Canagaratna, M. R., Drewnick, F., Allan, J. D., Alfarra, M. R., Middlebrook, A. M., Slowik, J.  
1208 G., Zhang, Q., Coe, H., and Jayne, J. T.: Comment on "The effects of molecular weight and thermal  
1209 decomposition on the sensitivity of a thermal desorption aerosol mass spectrometer", *Aerosol Science*  
1210 *and Technology*, 50, i-xv, 2016.

1211 Jiménez, P. A., Dudhia, J., González-Rouco, J. F., Navarro, J., Montávez, J. P., and García-Bustamante, E.:  
1212 A revised scheme for the WRF surface layer formulation, *Monthly weather review*, 140, 898-918, 2012.

1213 Kaiser, J., Heil, A., Andreae, M., Benedetti, A., Chubarova, N., Jones, L., Morcrette, J.-J., Razinger, M.,  
1214 Schultz, M., and Suttie, M.: Biomass burning emissions estimated with a global fire assimilation system  
1215 based on observed fire radiative power, *Biogeosciences*, 9, 527-554, 2012.

1216 Kiley, C. M., Fuelberg, H. E., Palmer, P. I., Allen, D. J., Carmichael, G. R., Jacob, D. J., Mari, C., Pierce, R. B.,  
1217 Pickering, K. E., and Tang, Y.: An intercomparison and evaluation of aircraft-derived and simulated CO  
1218 from seven chemical transport models during the TRACE-P experiment, *Journal of Geophysical Research:*  
1219 *Atmospheres*, 108, 2003.

1220 Kumar, R., Peuch, V.-H., Crawford, J. H., and Brasseur, G.: Five steps to improve air-quality forecasts, in,  
1221 *Nature Publishing Group*, 2018.

1222 Longo, K., Freitas, S., Andreae, M., Yokelson, R., and Artaxo, P.: Biomass burning in Amazonia: Emissions,  
1223 long-range transport of smoke and its regional and remote impacts, *Amazonia and Global Change*, 186,  
1224 207-232, 2009.

1225 Longo, K., Freitas, S., Andreae, M., Setzer, A., Prins, E., and Artaxo, P.: The Coupled Aerosol and Tracer  
1226 Transport model to the Brazilian developments on the Regional Atmospheric Modeling System (CATT-  
1227 BRAMS)–Part 2: Model sensitivity to the biomass burning inventories, *Atmospheric Chemistry and*  
1228 *Physics*, 10, 5785-5795, 2010.

1229 Martin, R. V., Jacob, D. J., Yantosca, R. M., Chin, M., and Ginoux, P.: Global and regional decreases in  
1230 tropospheric oxidants from photochemical effects of aerosols, *Journal of Geophysical Research:*  
1231 *Atmospheres*, 108, 2003.

1232 McClure, C. D., and Jaffe, D. A.: US particulate matter air quality improves except in wildfire-prone areas,  
1233 *Proceedings of the National Academy of Sciences*, 115, 7901-7906, 2018.

1234 Middlebrook, A. M., Bahreini, R., Jimenez, J. L., and Canagaratna, M. R.: Evaluation of composition-  
1235 dependent collection efficiencies for the aerodyne aerosol mass spectrometer using field data, *Aerosol*  
1236 *Science and Technology*, 46, 258-271, 2012.

1237 Natarajan, M., Pierce, R. B., Schaack, T. K., Lenzen, A. J., Al-Saadi, J. A., Soja, A. J., Charlock, T. P., Rose, F.  
1238 G., Winker, D. M., and Worden, J. R.: Radiative forcing due to enhancements in tropospheric ozone and  
1239 carbonaceous aerosols caused by Asian fires during spring 2008, *Journal of Geophysical Research:*  
1240 *Atmospheres*, 117, 2012.

1241 Olson, J. S., Watts, J. A., and Allison, L. J.: Major World Ecosystem Complexes Ranked by Carbon in Live  
1242 Vegetation: A Database (revised November 2000), NDP-017, 2000.

1243 Pausas, J. G., and Ribeiro, E.: Fire and plant diversity at the global scale, *Global Ecology and*  
1244 *Biogeography*, 26, 889-897, 2017.



1245 Pausas, J. G., and Keeley, J. E.: Wildfires as an ecosystem service, *Frontiers in Ecology and the*  
1246 *Environment*, 17, 289-295, 2019.

1247 Pechony, O., and Shindell, D. T.: Driving forces of global wildfires over the past millennium and the  
1248 forthcoming century, *Proceedings of the National Academy of Sciences*, 107, 19167-19170, 2010.

1249 Perring, A. E., Schwarz, J. P., Markovic, M. Z., Fahey, D. W., Jimenez, J. L., Campuzano-Jost, P., Palm, B.  
1250 D., Wisthaler, A., Mikoviny, T., and Diskin, G.: In situ measurements of water uptake by black carbon-  
1251 containing aerosol in wildfire plumes, *Journal of Geophysical Research: Atmospheres*, 122, 1086-1097,  
1252 2017.

1253 Peterson, D. A., Hyer, E. J., Campbell, J. R., Solbrig, J. E., and Fromm, M. D.: A conceptual model for  
1254 development of intense pyrocumulonimbus in western North America, *Monthly Weather Review*, 145,  
1255 2235-2255, 2017.

1256 Pierce, R., Al-Saadi, J., Schaack, T., Lenzen, A., Zapotocny, T., Johnson, D., Kittaka, C., Buker, M.,  
1257 Hitchman, M., and Tripoli, G.: Regional Air Quality Modeling System (RAQMS) predictions of the  
1258 tropospheric ozone budget over east Asia, *Journal of Geophysical Research: Atmospheres*, 108, 2003.

1259 Pierce, R. B., Schaack, T., Al-Saadi, J. A., Fairlie, T. D., Kittaka, C., Lingenfeller, G., Natarajan, M., Olson, J.,  
1260 Soja, A., and Zapotocny, T.: Chemical data assimilation estimates of continental US ozone and nitrogen  
1261 budgets during the Intercontinental Chemical Transport Experiment–North America, *Journal of*  
1262 *Geophysical Research: Atmospheres*, 112, 2007.

1263 Pierce, R. B., Al-Saadi, J., Kittaka, C., Schaack, T., Lenzen, A., Bowman, K., Szykman, J., Soja, A., Ryerson,  
1264 T., and Thompson, A. M.: Impacts of background ozone production on Houston and Dallas, Texas, air  
1265 quality during the Second Texas Air Quality Study field mission, *Journal of Geophysical Research:*  
1266 *Atmospheres*, 114, 2009.

1267 Powers, J. G., Klemp, J. B., Skamarock, W. C., Davis, C. A., Dudhia, J., Gill, D. O., Coen, J. L., Gochis, D. J.,  
1268 Ahmadov, R., and Peckham, S. E.: The weather research and forecasting model: Overview, system  
1269 efforts, and future directions, *Bulletin of the American Meteorological Society*, 98, 1717-1737, 2017.

1270 Prins, E., Schmetz, J., Flynn, L., Hillger, D., and Feltz, J.: Overview of current and future diurnal active fire  
1271 monitoring using a suite of international geostationary satellites. *Global and Regional Wildfire*  
1272 *Monitoring: Current Status and Future Plans*, in, SPB Academic publishing, 2001.

1273 Prins, E. M., and Menzel, W. P.: Geostationary satellite detection of bio mass burning in South America,  
1274 *International Journal of Remote Sensing*, 13, 2783-2799, 1992.

1275 Prins, E. M., and Menzel, W. P.: Trends in South American biomass burning detected with the GOES  
1276 visible infrared spin scan radiometer atmospheric sounder from 1983 to 1991, *Journal of Geophysical*  
1277 *Research: Atmospheres*, 99, 16719-16735, 1994.

1278 Prins, E. M., Feltz, J. M., Menzel, W. P., and Ward, D. E.: An overview of GOES-8 diurnal fire and smoke  
1279 results for SCAR-B and 1995 fire season in South America, *Journal of Geophysical Research:*  
1280 *Atmospheres*, 103, 31821-31835, 1998.

1281 Reid, C. E., Brauer, M., Johnston, F. H., Jerrett, M., Balmes, J. R., and Elliott, C. T.: Critical review of health  
1282 impacts of wildfire smoke exposure, *Environmental health perspectives*, 124, 1334-1343, 2016.

1283 Reid, J. S., Hyer, E. J., Prins, E. M., Westphal, D. L., Zhang, J., Wang, J., Christopher, S. A., Curtis, C. A.,  
1284 Schmidt, C. C., and Eleuterio, D. P.: Global monitoring and forecasting of biomass-burning smoke:  
1285 Description of and lessons from the Fire Locating and Modeling of Burning Emissions (FLAMBE) program,  
1286 *IEEE Journal of Selected Topics in Applied Earth Observations and Remote Sensing*, 2, 144-162, 2009.

1287 Roberts, J., Trainer, M., Murphy, D., Brown, S., Brewer, A., Gao, R.-S., and Fahey, D.: Fire Influence on  
1288 Regional to Global Environments and Air Quality (FIREX-AQ), in, 2018.

1289 Schaack, T. K., Zapotocny, T. H., Lenzen, A. J., and Johnson, D. R.: Global climate simulation with the  
1290 University of Wisconsin global hybrid isentropic coordinate model, *Journal of climate*, 17, 2998-3016,  
1291 2004.

1292 Schmidt, C. C., and Prins, E. M.: GOES wildfire ABBA applications in the western hemisphere, 2nd  
1293 International Wildland Fire Ecology and Fire Management Congress, AMS 5th Symposium Fire and  
1294 Forest Meteorology, (November), 2003.

1295 Schwarz, J., Spackman, J., Gao, R., Perring, A., Cross, E., Onasch, T., Ahern, A., Wrobel, W., Davidovits, P.,  
1296 and Olfert, J.: The detection efficiency of the single particle soot photometer, *Aerosol science and  
1297 technology*, 44, 612-628, 2010a.

1298 Schwarz, J., Spackman, J., Gao, R., Watts, L., Stier, P., Schulz, M., Davis, S., Wofsy, S. C., and Fahey, D.:  
1299 Global-scale black carbon profiles observed in the remote atmosphere and compared to models,  
1300 *Geophysical Research Letters*, 37, 2010b.

1301 Schwarz, J. P., Gao, R., Fahey, D., Thomson, D., Watts, L., Wilson, J., Reeves, J., Darbeheshti, M.,  
1302 Baumgardner, D., and Kok, G.: Single-particle measurements of midlatitude black carbon and light-  
1303 scattering aerosols from the boundary layer to the lower stratosphere, *Journal of Geophysical Research:*  
1304 *Atmospheres*, 111, 2006.

1305 Schwarz, J. P., Gao, R., Spackman, J., Watts, L., Thomson, D., Fahey, D., Ryerson, T., Peischl, J., Holloway,  
1306 J., and Trainer, M.: Measurement of the mixing state, mass, and optical size of individual black carbon  
1307 particles in urban and biomass burning emissions, *Geophysical Research Letters*, 35, 2008.

1308 Schwarz, J. P., Weinzierl, B., Samset, B. H., Dollner, M., Heimerl, K., Markovic, M. Z., Perring, A. E., and  
1309 Ziemba, L.: Aircraft measurements of black carbon vertical profiles show upper tropospheric variability  
1310 and stability, *Geophysical Research Letters*, 44, 1132-1140, 2017.

1311 Seiler, W., and Crutzen, P. J.: Estimates of gross and net fluxes of carbon between the biosphere and the  
1312 atmosphere from biomass burning, *Climatic change*, 2, 207-247, 1980.

1313 Sestini, M., Reimer, E., Valeriano, D., Alvalá, R., Mello, E., Chan, C., and Nobre, C.: Mapa de cobertura da  
1314 terra da Amazônia legal para uso em modelos meteorológicos, *Anais XI Simpósio Brasileiro de  
1315 Sensoriamento Remoto*, 2901-2906, 2003.

1316 Skamarock, W. C., Klemp, J. B., Dudhia, J., Gill, D. O., Liu, Z., Berner, J., Wang, W., Powers, J. G., Duda, M.  
1317 G., and Barker, D. M.: A description of the advanced research WRF model version 4, *National Center for  
1318 Atmospheric Research: Boulder, CO, USA*, 145, 2019.

1319 Stith, J., Ramanathan, V., Cooper, W., Roberts, G., DeMott, P., Carmichael, G., Hatch, C., Adhikary, B.,  
1320 Twohy, C., and Rogers, D.: An overview of aircraft observations from the Pacific Dust Experiment  
1321 campaign, *Journal of Geophysical Research: Atmospheres*, 114, 2009.

1322 Sullivan, J. T., McGee, T. J., Thompson, A. M., Pierce, R. B., Sumnicht, G. K., Twigg, L. W., Eloranta, E., and  
1323 Hoff, R. M.: Characterizing the lifetime and occurrence of stratospheric-tropospheric exchange events in  
1324 the rocky mountain region using high-resolution ozone measurements, *Journal of Geophysical Research:*  
1325 *Atmospheres*, 120, 12410-12424, 2015.

1326 Thompson, G., Rasmussen, R. M., and Manning, K.: Explicit forecasts of winter precipitation using an  
1327 improved bulk microphysics scheme. Part I: Description and sensitivity analysis, *Monthly Weather  
1328 Review*, 132, 519-542, 2004.

1329 Thompson, G., Field, P. R., Rasmussen, R. M., and Hall, W. D.: Explicit forecasts of winter precipitation  
1330 using an improved bulk microphysics scheme. Part II: Implementation of a new snow parameterization,  
1331 *Monthly Weather Review*, 136, 5095-5115, 2008.

1332 Val Martin, M., Kahn, R. A., Logan, J. A., Paugam, R., Wooster, M., and Ichoku, C.: Space-based  
1333 observational constraints for 1-D fire smoke plume-rise models, *Journal of Geophysical Research:*  
1334 *Atmospheres*, 117, 2012.

1335 Van Der Werf, G. R., Randerson, J. T., Collatz, G. J., Giglio, L., Kasibhatla, P. S., Arellano, A. F., Olsen, S. C.,  
1336 and Kasischke, E. S.: Continental-scale partitioning of fire emissions during the 1997 to 2001 El Nino/La  
1337 Nina period, *Science*, 303, 73-76, 2004.

1338 van der Werf, G. R., Randerson, J. T., Giglio, L., Collatz, G. J., Kasibhatla, P. S., and Arellano Jr, A. F.:  
1339 Interannual variability in global biomass burning emissions from 1997 to 2004, *Atmospheric Chemistry  
1340 and Physics*, 6, 3423-3441, 2006.

1341 Van der Werf, G. R., Randerson, J. T., Giglio, L., Collatz, G., Mu, M., Kasibhatla, P. S., Morton, D. C.,  
1342 DeFries, R., Jin, Y. v., and van Leeuwen, T. T.: Global fire emissions and the contribution of deforestation,  
1343 savanna, forest, agricultural, and peat fires (1997–2009), *Atmospheric chemistry and physics*, 10, 11707-  
1344 11735, 2010.

1345 Van Der Werf, G. R., Randerson, J. T., Giglio, L., Van Leeuwen, T. T., Chen, Y., Rogers, B. M., Mu, M., Van  
1346 Marle, M. J., Morton, D. C., and Collatz, G. J.: Global fire emissions estimates during 1997–2016, *Earth  
1347 System Science Data*, 9, 697-720, 2017.

1348 Wang, X., and Lei, T.: GSI-based four-dimensional ensemble–variational (4DensVar) data assimilation:  
1349 Formulation and single-resolution experiments with real data for NCEP Global Forecast System, *Monthly  
1350 Weather Review*, 142, 3303-3325, 2014.

1351 Wesely, M.: Parameterization of surface resistances to gaseous dry deposition in regional-scale  
1352 numerical models, *Atmospheric Environment*, 23, 1293-1304, 1989.

1353 Wiedinmyer, C., Akagi, S., Yokelson, R. J., Emmons, L., Al-Saadi, J., Orlando, J., and Soja, A.: The Fire  
1354 INventory from NCAR (FINN): A high resolution global model to estimate the emissions from open  
1355 burning, *Geoscientific Model Development*, 4, 625-641, 2011.

1356 Wiggins, E. B., Soja, A. J., Gargulinski, E., Halliday, H. S., Pierce, R. B., Schmidt, C. C., Nowak, J. B.,  
1357 DiGangi, J. P., Diskin, G. S., and Katich, J. M.: High temporal resolution satellite observations of fire  
1358 radiative power reveal link between fire behavior and aerosol and gas emissions, *Geophysical Research  
1359 Letters*, 47, e2020GL090707, 2020.

1360 Wiggins, E. B., Anderson, B., Brown, M., Campuzano-Jost, P., Chen, G., Crawford, J., Crosbie, E., Dibb, J.,  
1361 DiGangi, J., and Diskin, G.: Reconciling Assumptions in Bottom-up and Top-down Approaches for  
1362 Estimating Aerosol Emission Rates from Wildland Fires using Observations from FIREX-AQ, *Journal of  
1363 Geophysical Research: Atmospheres*, e2021JD035692, 2021.

1364 Xu, L., Crouse, J. D., Vasquez, K. T., Allen, H., Wennberg, P. O., Bourgeois, I., Brown, S. S., Campuzano-  
1365 Jost, P., Coggon, M. M., and Crawford, J. H.: Ozone chemistry in western US wildfire plumes, *Science  
1366 advances*, 7, eabl3648, 2021.

1367 Xu, R., Yu, P., Abramson, M. J., Johnston, F. H., Samet, J. M., Bell, M. L., Haines, A., Ebi, K. L., Li, S., and  
1368 Guo, Y.: Wildfires, global climate change, and human health, *New England Journal of Medicine*, 383,  
1369 2173-2181, 2020.

1370 Xu, W., Lambe, A., Silva, P., Hu, W., Onasch, T., Williams, L., Croteau, P., Zhang, X., Renbaum-Wolff, L.,  
1371 and Fortner, E.: Laboratory evaluation of species-dependent relative ionization efficiencies in the  
1372 Aerodyne Aerosol Mass Spectrometer, *Aerosol Science and Technology*, 52, 626-641, 2018.

1373 Yates, E., Iraci, L., Roby, M., Pierce, R., Johnson, M., Reddy, P., Tadić, J., Loewenstein, M., and Gore, W.:  
1374 Airborne observations and modeling of springtime stratosphere-to-troposphere transport over  
1375 California, *Atmospheric Chemistry and Physics*, 13, 12481-12494, 2013.

1376 Ye, X., Arab, P., Ahmadov, R., James, E., Grell, G. A., Pierce, B., Kumar, A., Makar, P., Chen, J., and  
1377 Davignon, D.: Evaluation and intercomparison of wildfire smoke forecasts from multiple modeling  
1378 systems for the 2019 Williams Flats fire, *Atmospheric Chemistry and Physics*, 21, 14427-14469, 2021.

1379